Repository of the Max Delbrück Center for Molecular Medicine (MDC) in the Helmholtz Association

https://edoc.mdc-berlin.de/21260/

Claudin-10a deficiency shifts proximal tubular Cl(-) permeability to cation selectivity via claudin-2 redistribution.

Breiderhoff, T., Himmerkus, N., Meoli, L., Fromm, A., Sewerin, S., Kriuchkova, N., Nagel, O., Ladilov, Y., Krug, S., Quintanova, C., Stumpp, M., Garbe-Schönberg, D., Westernströer, U., Merkel, C., Brinkhus, M., Altmüller, J., Schweiger, M., Mueller, D., Mutig, K., Morawski, M., Halbritter, J., Milatz, S., Bleich, M., Günzel, D.

Title:

Claudin-10a deficiency shifts proximal tubular Cl- permeability to cation selectivity via claudin-2 redistribution

Authors

Tilman Breiderhoff[1]*, Nina Himmerkus[2]*, Luca Meoli[3], Anja Fromm[3], Sebastian Sewerin[4], Natalia Kriuchkova[5], Oliver Nagel[3], Yury Ladilov[3], Susanne M. Krug[3], Catarina Quintanova[2], Meike Stumpp[6], Dieter Garbe-Schönberg[7], Ulrike Westernströer[7], Cosima Merkel[2], Merle Annette Brinkhus[2], Janine Altmüller[8,9], Michal R. Schweiger[8,10], Dominik Müller[1], Kerim Mutig[5], Markus Morawski[11], Jan Halbritter[4], Susanne Milatz[2], Markus Bleich[2]**, Dorothee Günzel[3]**

*, **, equally contributing

[1]Department of Pediatrics, Division of Gastroenterology, Nephrology and Metabolic Medicine, Charité – Universitätsmedizin Berlin, Augustenburger Platz 1, 13353 Berlin, Germany

[2]Institute of Physiology, Christian-Albrechts-Universität zu Kiel, Hermann-Rodewald-Straße 5, 24118 Kiel, Germany

[3]Clinical Physiology / Div. of Nutritional Medicine, Charité – Universitätsmedizin Berlin, Hindenburgdamm 30, 12203 Berlin, Germany

[4]Division of Nephrology, University of Leipzig Medical Center, Liebigstr. 20, 04103 Leipzig, Germany.

[5]Institute for Functional Anatomy, Charité – Universitätsmedizin Berlin, Philipstraße 11, 10115 Berlin, Germany

[6]Zoological Institute, Comparative Immunobiology, Christian-Albrechts-Universität zu Kiel, Am Botanischen Garten 1-9, 24118 Kiel, Germany

[7]Institute of Geosciences, Christian-Albrechts-Universität zu Kiel, Ludewig-Meyn-Str. 10, 24118 Kiel, Germany

[8]Cologne Center for Genomics, University of Cologne, Weyertal 115b, 50931 Köln, Germany

[9]Berlin Institute of Health at Charité, Core Facility Genomics, Berlin, Germany & Max Delbrück Center for Molecular Medicine in the Helmholtz Association, Berlin, Germany

[10]Institute for Translational Epigenetics, University Hospital Cologne, University of Cologne, Weyertal 115, 50931 Köln & Center for Molecular Medicine Cologne, CMMC, Medical Faculty, University of Cologne, Robert-Koch-Str.21, 50931 Köln

[11]Paul Flechsig Institute of Brain Research, University of Leipzig, Liebigstr. 19, 04103 Leipzig, Germany & Department of Neurophysics, Max Planck Institute for Human Cognitive and Brain Sciences, Stephanstr. 1a, 04103 Leipzig, Germany

Running Title

Claudin-10a deficiency

Corresponding Author's Name, Address, and E-Mail Information,

Prof. Dr. Dorothee Günzel
Clinical Physiology / Div. of Nutritional Medicine
Charité – Universitätsmedizin Berlin
Hindenburgdamm 30
12203 Berlin
Germany
dorothee.guenzel@charite.de

Key Words

paracellular ion transport, tight junction, proximal tubule, chloride, magnesium, kidney, knockout mouse

Significance Statement

Claudin-10 is a tight junction protein expressed along the nephron. Isoform claudin-10b facilitates paracellular Na^+ transport in the thick ascending limb. This study demonstrates that isoform claudin-10a is essential for paracellular Cl^- transport in the proximal tubule. In mice lacking claudin-10a, additional cation-selective claudin-2 incorporates into proximal tubule tight junctions. This turns paracellular anion into cation preference with renal retention of calcium and magnesium, and hypermagnesemia. Loss of anion permeability is compensated already within the proximal tubule and in more distal parts of the nephron. Human HELIX syndrome arises from mutations in the *CLDN10* gene that affect either claudin-10b or both isoforms. Data from the claudin-10a deficient mouse suggest that mutations affecting both isoforms result in more severe electrolyte imbalance.

ABSTRACT

Background: The tight junction (TJ) proteins claudin-2 and -10a form paracellular cation and anion channels, respectively, and are expressed in the proximal tubule (PT). However, the physiological role of claudin-10a in the kidney is yet obscure.

Methods: Mice deficient in claudin-10a were generated and successful knockout was confirmed by Southern Blot, Western Blot, and immunofluorescence staining. Urine and serum of knockout and wild-type animals were analyzed. The functionality of isolated PTs was investigated electrophysiologically. Compensatory regulation was studied by pharmacological intervention, RNA-Seq analysis, Western Blot, immunofluorescence staining, and respirometry.

Results: Mice deficient in claudin-10a were fertile and without overt phenotypes. Upon knockout, claudin-10a was replaced by claudin-2 in all PT segments. Electrophysiology showed conversion from paracellular anion to cation preference and a loss of paracellular Cl^- over HCO_3^- preference. In consequence there was tubular retention of calcium and magnesium, higher urine pH and mild hypermagnesemia. Other urine and serum parameters under control conditions and sequential pharmacological transport inhibition, as well as unchanged fractional lithium excretion suggested proximal and distal tubular compensation. Changes in proximal tubular O_2 handling and differential expression of genes regulating fatty acid metabolism indicated proximal tubular adaptation. Western Blot and immunofluorescence revealed alterations in distal tubular transport.

Conclusions: Claudin-10a is the major paracellular anion channel in the PT. Deletion causes calcium and magnesium hyperreabsorption by claudin-2 redistribution. Loss of paracellular anion permeability is compensated by transcellular transport in proximal and distal segments and proximal tubular metabolic adaptation.

INTRODUCTION

Claudins are a family of tetraspan membrane proteins and essential constituents of the tight junction (TJ) in epithelia and endothelia.[1,for rev. 2] Whereas many claudins simply tighten the paracellular cleft, some claudins convey specific ion and water permeabilities to the paracellular pathway, i.e., act as paracellular channels.[for rev. 3-5] Claudin-10a, a paracellular anion channel,[6,7] and claudin-10b, a cation channel without water permeability,[6-8] are encoded by *Cldn10*. They result from the alternative use of two different promotors, leading to the expression of exon 1a or exon 1b. They differ in their 71 (claudin-10a) and 73 (claudin-10b) N-terminal amino acids, respectively, but share 155 C-terminal amino acids.

According to segment-specific expression analyses, claudin-10 is expressed in the proximal tubule (PT) together with claudin-2.[9-11] Claudin-10 is further expressed in the TAL, a segment that also shows high expression for claudin-16 and -19. Several studies indicate that claudin-10 in the PT is exclusively claudin-10a, whereas in the TAL, claudin-10b is expressed.[6,7,12,13]

Usually, several different claudins form a functional TJ strand. This allows the constitution of specific paracellular permeability features by the combination of the individual tightening and permeating properties of the respective claudin proteins. In murine proximal convoluted tubules, a slight paracellular anion preference was reported.[14] In contrast, others described a slight cation preference in PT S2 and S3 (proximal straight tubule, PST), respectively.[15,16]

The roles of claudin-2 and claudin-12 in the PT have been described in detail. Claudin-2 acts as a paracellular channel for mono- and divalent cations and water.[8,17,18] Muto et al. demonstrated that claudin-2 deficiency led to a shift from cation preference to a slight preference for anions in PT S2.[15] PST from mice deficient for claudin-12 had similar properties.[16] Both mouse models only showed metabolic alterations after dietary challenge.[15,16] The importance of the paracellular pathway was demonstrated by the increased energy expenditure of the kidney, necessary to compensate for claudin-2 deficiency in the proximal tubule.[19]

Patients with mutations in the *CLDN10* gene suffer from HELIX syndrome, i.e., hypohydrosis, electrolyte imbalance (polyuria, hypermagnesemia, hypocalciuria, and in some patients hypokalemia), lacrimal gland dysfunction, ichthyosis, and xerostomia.[20-25] Similar electrolyte imbalances have already been described for mice lacking claudin-10 in TAL and distal nephron segments.[12] Mutations in patients suffering from HELIX syndrome known to date affect either claudin-10b or both claudin-10 isoforms, whereas patients with specific claudin-10a mutations have not yet been described.[for rev. 26]

The present study aims to

(i) clarify claudin expression and paracellular properties along the proximal tubule, either expressing or lacking claudin-10a.

(ii) investigate the physiological role of claudin-10a in a mouse knockout model.

(iii) evaluate any new finding in the frame of the main clinical features of the HELIX syndrome.

METHODS

Animal Housing and Handling

All experiments were performed in accordance with the German law on animal protection (*Landesamt für Gesundheit und Soziales* (LAGeSo), Berlin G0121/13 and T0256/16; Ministerium für Energiewende, Landwirtschaft, Umwelt, Natur und Digitalisierung des Landes Schleswig-Holstein and animal welfare officer of Christian-Albrechts-University Kiel, animal ethics protocol number V312-72241.121-2).

Animals used in the experiments were either mice (8 - 12 weeks old) from homozygous breedings using age matched controls or littermates from heterozygous breedings. Mice were housed under standardized conditions (12 hr light/dark cycle; 22–24°C temperature; 55% ± 15% humidity; *ad libitum* access to standard diet and water).

Generation of Cldn10a deficient mice

For homologous recombination in embryonic stem cells, a targeting vector was constructed as schematically shown in supplemental Fig. S1. Briefly, homologous regions to the murine *Cldn10* Exon1a locus were amplified by PCR from ES cell DNA (129 SvEv,[1]) using oligonucleotides listed in supplemental Table S1. A loxP site was inserted 433 bp upstream of exon 1a and an FRT/loxP site flanked puromycin cassette was inserted 317 bp downstream of exon 1a. After electroporation of the linearized construct into ES cells and selection with puromycin, cells with homologous recombination were screened and confirmed by Southern Blot using PstI and BglII restriction enzymes and an external probe (Fig. S1). Mice derived from these cells were bred to Cre recombinase expressing mice (B6.C-Tg(CMV-cre)1Cgn/J, The Jackson Laboratory) to remove the puromycin cassette and generate mice heterozygous for the deleted *Cldn10a* allele (*Cldn10a*$^{+/-}$). These mice were backcrossed for more than ten generations to C57Bl/6NCrl (Charles River Laboratory).

Metabolic cage experiments

Acetazolamide: Mice were placed in metabolic cages overnight for about 17 hours. Urine was collected, as well as drinking volume measured. Blood was taken from the facial vein. Over the following 5 days, the animals were i.p. injected with 50 mg/kg BW acetazolamide in 0.9% sterile NaCl solution (5 µl/g body weight (BW)) daily. On the 5th day, the animals were again placed in metabolic cages overnight (17 hours). On the following day blood was taken from the facial vein and mice were sacrificed by cervical dislocation.

Furosemide and Hydrochlorothiazide: Animals were i.p. injected with vehicle or with 40 mg/kg BW furosemide in 0.9% sterile NaCl solution or with 100 mg/kg BW hydrochlorothiazide (5 µl/g BW) and placed in metabolic cages for 4 hours. Urine was collected, as well as drinking volume measured. After the 4 hours period, mice were sacrificed by terminal blood collection and decapitation under deep anesthesia (5% isoflurane).

In all experiments, blood and urine were analyzed for pH and electrolytes.

Tubule isolation

Cldn10a KO mice were sacrificed by terminal blood collection and decapitation under deep anesthesia (5% isoflurane). Spot urine was sampled if available. Kidneys were removed immediately. After decapsulation thin transversal slices were cut for either enzymatic tubule preparation or kept in incubation solution on ice for electrophysiological measurements. Enzymatic tubule preparation for molecular biology was performed as follows: thin transversal slices were digested in incubation solution (in mM: 140 NaCl, 0.4 KH_2PO_4, 1.6 K_2HPO_4, 1 $MgSO_4$, 10 sodium acetate, 1 α-ketoglutarate, 1.3 calcium gluconate, 5 glycine, pH 7.4, containing 48 µg/ml trypsin inhibitor and 25 µg/ml DNase I) with 2 mg/ml collagenase II (PAN-Biotech, Aidenbach, Germany) at 37°C and 850 rpm in a thermoshaker for 15 – 25 min. After vigorous washing in sorting solution (incubation solution supplemented with 0.5 µg/ml bovine serum albumin) tubules were transferred to stereomicroscopes (Leica, Wetzlar, Germany) and sorted at 4°C according to morphological criteria.[27-29] For RNA preparation 10 PCTs and approx. 20 DCTs per kidney were pooled, snap frozen and stored at -80°C until further processing for RNA-Seq. For Western Blot analysis 15 PCT or 15 PST tubules were mixed with 5 x Laemmli buffer and stored at -80°C until further use.

Blood and urine electrolyte measurements

Urine osmolarity was determined with a Wescor 5100B (South Logan, UT, USA) vapor pressure osmometer. Electrolyte concentrations from urine and serum sampled during metabolic cage experiments were measured with an ABL800 FLEX blood gas analyzer (Radiometer, Brønshøj, Denmark). Urine pH was determined with a pH meter (HI 9017, Hanna Instruments Deutschland GmbH, Vöhringen, Germany), urine and serum creatinine and urea concentrations were determined with Reflotron Plus (Hoffmann-La Roche, Basel, Switzerland). For serum creatinine determination 15 µl 2 mg/dl creatinine standard solution (DiaSys Diagnostic Systems GmbH, Holzheim, Germany) were added to 25 µl serum to bring the concentration within the measuring range of the equipment. Results were corrected accordingly.

Plasma and spot urine from mice sacrificed for electrophysiology series 1 or tubular molecular biology were analyzed for electrolytes by ion-selective electrodes and photometry, and for creatinine concentrations by ELISA (Hitachi Analyzer; Institute of Clinical Chemistry, UKSH Kiel, Germany). Spot urine pH was estimated by Neutralit® pH sticks (Merck, Darmstadt, Germany).

Serum and spot urine from mice sacrificed for electrophysiology series 2 as well as a pooled serum and urine samples of C57Bl/6N animals as standard controls and blank (H_2O) controls were precipitated by adding the same volume of trichloroacetic acid (Carl Roth, Germany). Precipitates were removed by centrifugation (20.000 x g) twice, discarding the pellet. Samples were analyzed by inductively coupled-mass-spectrometry (ICP-MS) using a quadrupole-based instrument (Agilent 7900) in no-gas mode. Prior to analysis samples were diluted 20-fold (Serum) or either 20-fold or 50-fold (urine) with 2 % (v/v) ultrapure nitric acid and spiked with 2.5 µg/L yttrium for internal standardization. Analytical results for lithium are blank-subtracted averages of 3 runs. Accuracy of the results was monitored by analyzing CRM's NIST 1643f Trace Elements in Water and Seronorm Trace Elements Serum L-2. Average precision of results was estimated from replicate analyses of in-house serum and urine standards being 0.7 and 3.5% RSD (1SD), respectively. In addition, serum and urine samples were analyzed by flame photometry (EFOX 5053, Eppendorf, Germany) twice, untreated and after trichloroacetic acid precipitation with no evident difference in outcome. Na, K, Ca and Li concentrations in urine and serum together with the respective creatinine values were used to calculate fractional excretions for all 4 cations.

Respirometry

To measure oxygen consumption of isolated proximal tubules, we adapted an established respiration protocol.[30] We used a 24-channel plate reader system (PreSens SDR SensorDish® Reader) with integrated oxygen sensor spots. The sensor spots are at the bottom of each well and are read out non-invasively through the transparent bottom of the well plate when placed on the SensorDish® reader. Calibration of oxygen sensors was performed by preparing oxygen-free and air-equilibrated water (100% air saturated). The oxygen-free water was prepared by dissolving 1% (w/v) sodium sulfite in distilled water to scavenge oxygen. Enzymatically sorted proximal convoluted tubules (PCT) of similar length (300-500 µm) were added to four wells and incubated with a minimal solution (in mM: 130 NaCl, 0.4 KH_2PO_4, 1.6 K_2HPO_4, 5 HEPES, 1 $MgCl_2$, 3 $CaCl_2$, 10 Na-Acetate, 5 Glycine and 5 NaOH to adjust pH to 7.4, equilibrated to room air) or DMEM cell culture medium (PAN-Biotech, low glucose, 5% CO_2). Four wells without tubules but with respective solutions were measured in parallel for background control. Each well was sealed by a gas-tight glass coverslip and the plate was maintained at 37 °C by a water heating system. Recordings of oxygen partial pressure (pO_2) were run every two minutes for 45 min, at 37 °C, to obtain the decrease in pO_2 inside the respiration chambers. Time points 5' to 25' where analyzed for the slope of oxygen consumption and the background slope was subtracted. The data was normalized to the amount of PCT in the chambers, 15 PCT incubated in the minimal solution and 5 PCT incubated in DMEM. Supplemental Fig. S2 shows calibration curves for both solutions, using 5, 10, 15 and 20 PCT in minimal solution and 2, 4, 6 and 8 PCT in DMEM. Decrease in pO_2 was used to calculate the respiration rate expressed as µmol O_2/h/tubule. For each mouse the relative increase in O_2 consumption between minimal solution and DMEM was calculated as measure of metabolic capacity.

Protein Extraction / SDS-PAGE / Western Blot

Membrane protein extraction from whole mouse kidney

Kidneys were decapsulated and tissue was homogenized with a Teflon homogenizer in 2 ml ice-cold homogenization buffer (140 mM NaCl, 20 mM Tris pH 7.4, 5 mM EDTA, and protease inhibitors (1 cOmplete[TM] EDTA free tablet; (Roche, Basel, Switzerland), 1 µM Pepstatin A and 2 PhosStop tablets (Roche)) on ice and centrifuged at 1000 × g for 10 min at 4°C. Supernatant was transferred to a new tube and centrifuged at 42100 × g for 45 min at 4°C. The pellet was resuspended in lysis buffer (50 mM Tris pH 6.8, 5 mM EDTA, 2% SDS, 1 complete Mini EDTA-free tablet, 1 µM Pepstatin A, 2 PhosStop tablets). Membrane protein concentration was quantified using bicinchoninic acid protein assay reagent (BCA; Pierce, Rockford, IL, USA) and a plate reader (Tecan, Zürich, Switzerland). 30 µg (for claudin detection) or 50 µg (all other

proteins) membrane protein lysate was mixed with 2 $\times$ Laemmli buffer and denatured at 37°C for 15 min.

Protein extraction from isolated PCT and PST kidney tubules

15 PCT or 15 PST tubules in Laemmli buffer (total volume of 20 µl) were denatured at 95°C for 5 min.

SDS Page and Western Blot

Proteins were separated on Any KD- or 4-15% Mini-PROTEAN® TGX Stain-Free™ Protein Gels (Bio-Rad Laboratories GmbH, Feldkirchen, Germany), and blotted for 7 min (small proteins) or 10 min (large proteins) with a Trans-Blot® Turbo™ Transfer System onto a PVDF membrane (Trans-Blot® Turbo™ Midi PVDF Transfer Packs). Proteins were detected using antibodies listed by ab # in supplementary Table S2: mouse anti-claudin-2 (#1) and rabbit anti-claudin-10 (#2), rabbit anti-aquaporin 2 (#3), rabbit anti-NKCC2 (#4), rabbit anti-pNCC (#5), rabbit anti-NCC (#6), mouse anti-β-actin (#7), and mouse anti-tubulin (loading control, #8). Peroxidase conjugated secondary antibodies (1:10000, Jackson) were used, followed by incubation in SuperSignal™ West Pico Plus, (Thermo Fisher Scientific, Waltham, USA) to detect bound primary antibodies. Signals were visualized by Fusion FX6 and FX7 chemiluminescence imaging system (Vilber Lourmat Deutschland GmbH, Eberhardzell, Germany). Densitometric analysis was performed using the AIDA Image Analyser (Raytest, Straubenhardt, Germany). For quantification Western Blot linearity with respect to protein concentration was validated (Fig. S3). Original Western Blots are shown in Fig. S4.

Quantitative PCR on RNA from isolated tubules and intestine

Total RNA was extracted from isolated tubules using TRIzol reagent (Life Technologies), purified by RNeasy Mini Kit (Qiagen, Hilden, Germany) and reverse transcribed using the High-Capacity cDNA Reverse Transcription Kit (Applied Biosystems, Waltham, USA). cDNA was amplified with PowerUp SYBR Green Mastermix (Applied Biosystems) on a Quantstudio 3 (Applied Biosystems) using the folling primers (5′ to 3′): mCldn10a: forward, CCGGCCACATTTCACTATCT, reverse GATCTGAGCCTCCGACTTTG, mCldn2: forward, GTCATCGCCCATCAGAAGAT, reverse, AGGGAACCAGTCTCCGTTCT; housekeeping gene mTbp: forward, CAAACCCAGAATTGTTCTCCTT, reverse, TGGTCTTCCTGAATCCCTTT. Gene expression was analysed using the comparative CT method and normalized to WT.

For gene expression analysis in the intestine, mice were sacrificed and the small intestine was divided into three segments of approximately equally length along the proximal-to-distal intestinal axis. Per each intestinal segment a distal fraction of about 2 cm representative of duodenum, jejunum and ileum, respectively, were dissected. Additionally, colon was isolated and dissected. RNA extraction and cDNA preparations were performed as described above. A TaqMan Real-Time PCR assay was performed using a 7500 Fast Real Time PCR System (Applied Biosystems). Probes for mCldn10a and mCldn10b isoforms were Mm07304888_m1 and Mm01226325_m1, respectively (Thermo Fisher Scientific). Probe for mouse Actb, used as the reference gene, was 4352341E (Applied Biosystems). Relative expression ratios of *Cldn10a* and *Cldn10b* to Actb were calculated and reported for both control and *Cldn10a* KO mice.

ELISA

Freshly prepared blood plasma was used to evaluate copeptin levels as a surrogate marker for circulating ADH (mouse copeptin ELISA kit Cloud-Clone Corp., Katy, TX, USA) according to the manufacturer's instructions.

Electrophysiology

Series 1: PT segments were isolated using a stereomicroscope (Leica) at 4°C and divided in 4 groups: S1 segments were identified by a still attached glomerulus which was cut off. Convoluted parts of the PT not attached to a glomerulus or harvested before entering a medullary ray were considered a mix of S1 and S2 and combined in one group named proximal convoluted tubule (PCT). S2 segments were harvested shortly before or after entering the medullary rays. S3/PST segments were taken from the outer stripe of outer medulla and showed a distinct cellular pattern (see also supplemental Fig. S5). In parallel, cortical TAL was dissected and characterized. PT and TAL segments were microperfused using a double-barrelled perfusion pipette as described previously.[31] All perfusions and recordings were conducted at 37°C. Transepithelial voltage was recorded during the whole experiment. Length and diameter of tubules were obtained from digitized images. PT were placed in and perfused with a physiological control solution (in mM: 140 NaCl, 5.4 KCl, 1 $MgCl_2$, 1.2 $CaCl_2$, 10 HEPES, 5 NaOH to adjust pH to 7.4). The transepithelial resistance was estimated using the cable equation, and equivalent short circuit current was calculated according to Ohm's law (Tables S3 to S5). To determine single ion permeabilities, diffusion potentials were obtained by consecutively replacing the peritubular bath solution by low-NaCl solution (in mM: 220 mannitol, 30 NaCl, 5.4 KCl, 1 $MgCl_2$, 1.2 $CaCl_2$, 10 mM HEPES, 5 NaOH to adjust pH to 7.4)

and high-HCO$_3^-$ solution (in mM 140 NaHCO$_3$, 5.4 KCl, 1 MgCl$_2$, 1.2 CaCl$_2$, 10 mM HEPES, freshly prepared out of a CO$_2$ equilibrated bicarbonate stock and HEPES buffer to provide the correct pH 7.4). All obtained potentials were corrected for their respective liquid junction potentials. Permeability ratios P$_{Na}$/P$_{Cl}$ and P$_{Cl}$/P$_{HCO_3}$ were calculated using the Goldman-Hodgkin-Katz equation. Whenever possible, perfused proximal tubules were retrieved after perfusion experiments and were transferred to glass slides where they were fixed (4% PFA in PBS) and washed in 0.3% Triton X-100 in PBS (PBS-T) under visual control, and immunofluorescence was performed.

Series 2: S1, PCT, S2 and S3/PST segments dissected as described above where investigated after replacement of chloride by pyruvate to investigate cation selectivity more independent of the high impact of loss of chloride permeability in the *Cldn10a* KO situation. The following Na-pyruvate control solution was used for luminal and basolateral perfusion (in mM): 145 Na-pyruvate, 5.4 K-pyruvate, 1 Mg-pyruvate, 1.2 Ca-pyruvate, 3 HEPES, 2.2 NaOH to adjust pH to 7.4. For the measurement of the Na-pyruvate diffusion potential basolateral low Na-pyruvate solution was used (in mM: 30 Na-pyruvate, 5.4 K-pyruvate, 1 Mg-pyruvate, 1.2 Ca-pyruvate, 3 HEPES, 2.2 NaOH to adjust pH to 7.4, 230 mannitol to adjust osmolality). In a last step, divalent bi-ionic diffusion potentials were measured by subsequent superfusion with high Mg-pyruvate solution (in mM: 5.4 K-pyruvate, 1 Mg-pyruvate, 1.2 Ca-pyruvate, 10 HEPES, 5.5 KOH to adjust pH to 7.4, 105 mannitol to adjust osmolality) followed by high Ca-Pyruvate solution (in mM: 5.4 K-pyruvate, 1 Mg-pyruvate, 95 Ca-pyruvate, 10 HEPES, 6 KOH to adjust pH to 7.4, 85 mannitol to adjust osmolality). Potentials were corrected for liquid junction potentials with an assumed relative ion mobility (U$_{pyruvate}$ /U$_K$) of 0.524 as mean of the relative mobilities of acetate, lactate and proprionate (https://medicalsciences.med.unsw.edu.au/research/research-services/ies/ionicmobilitytables). Permeability ratios P$_{Na}$/P$_{Pyr}$, P$_{Mg}$/P$_{Pyr}$ and P$_{Ca}$/P$_{Pyr}$ were calculated accordingly. P$_{Cl}$/P$_{Pyr}$ was estimated by using the respective median value of the previous calculated P$_{Na}$/P$_{Cl}$ values, for each segment and genotype. Similarly, P$_{HCO_3}$/P$_{Pyr}$ was estimated from the previously obtained P$_{HCO_3}$/P$_{Na}$ values.

To evaluate proximal tubular paracellular lithium handling by *Cldn10a* KO five S2 segments each of 4 WT and 4 KO animals were investigated for sodium-lithium diffusion potentials at the end of the experimental time frame for the pyruvate experiments (2h). S2 segments were perfused and superfused with control solution (in mM: 145 NaCl, 0.4 KH$_2$PO$_4$, 1.6 K$_2$HPO$_4$, 5 glucose, 1 MgCl$_2$, 1.3 Ca-gluconate, pH7.4) followed by NaCl diffusion potential measurement (basolateral 30 mM NaCl solution in mM: 30 NaCl, 0.4 KH$_2$PO$_4$, 1.6 K$_2$HPO$_4$, 5 glucose, 1 MgCl$_2$, 1.3 Ca-gluconate, 230 mannitol, pH7.4). After short re-application of control solution, the bi-ionic sodium-lithium diffusion potential was measured by basolateral replacement of the

control solution with a respective lithium solution (in mM: 145 LiCl, 0.4 KH_2PO_4, 1.6 K_2HPO_4, 5 glucose, 1 $MgCl_2$, 1.3 Ca-gluconate, pH7.4). Permeability ratios P_{Na}/P_{Cl} and P_{Na}/P_{Li} were calculated using the Goldman-Hodgkin-Katz equation, and P_{Li}/P_{Pyr} as described for the other ions.

Immunofluorescence Staining

Single PT segments (post-perfusion, post-fixation) were incubated with first antibodies (ab #, Table S2) rabbit anti-claudin-2 (#9) and mouse anti-claudin-10 (#10), both 1:400, overnight in PBS-T with 5% BSA. After vigorous washing with PBS-T under visual control, PTs were incubated with secondary antibodies (#11, #12) and finally mounted with Mowiol-DABCO-DAPI. Staining was visualized using a Zeiss LSM780 confocal microscope.

Mouse kidney sections were dewaxed and boiled in citrate buffer (pH 6) for antigen retrieval. Unspecific protein interactions were blocked using 5% skim milk for 30 min prior to the incubation with primary antibodies against claudin-1 (#13), claudin-2 (#14), claudin-10 (#15), claudin-12 antibody (#16), NaPi-IIa (#17), NHE3 (#18), NKCC2 (#19), NCC (#20), phosphorylated NCC (#21), or AQP2 (#22). After incubation with primary antibodies for 1 h at room temperature followed by 4°C overnight kidney sections were rinsed in PBS and incubated with respective Cy3- or Cy2-conjugated secondary antibodies (#23-#26) for 1h at room temperature, washed in PBS, covered, and evaluated by confocal microscopy (Zeiss LSM 5 Exciter and Zeiss LSM780).

For Cldn2/Occludin and Cldn2/ZO-1 co-staining and quantification, Mouse kidney sections were dewaxed and boiled in tris(hydroxymethyl)aminomethane (2 mmol/l), ethylenediamine tetraacetic acid (1.3 mmol/l), sodium citrate (1 mmol/l) buffer (Tris-EDTA-Citrate buffer, pH 7.8; microwave, 360 W, 3 x 10 min). Sections were blocked (4% goat serum in phosphate-buffered saline for 1 h) and incubated with primary antibodies (claudin-2 #14, occludin #27, ZO-1 #28) diluted in blocking solution at 4°C overnight. After multiple rinsing in PBS, sections were incubated with AlexaFluor 488- and AlexaFluor 594-conjugated secondary antibodies (#29, #30) and DAPI (4',6-diamidino-2-phenylindole dihydrochloride, Roche, stock 1 mg/ml methanol, 1:1000) for 1h at room temperature, washed in PBS and distilled water, mounted in ProTaqs Mount Fluor (Biocyc GmbH & Co KG, Potsdam, Germany) and evaluated by confocal microscopy (Zeiss LSM780) using the co-localization tool of the Zeiss ZEN software.

To estimate co-localization between occludin-positive vesicles and claudin-2, images were recorded from regions predominantly containing S1 segments. Intensity thresholds of 100 (total intensity range of 0 – 255) were chosen for both channels, resulting in three pixel areas per image: area 1, high occludin, low claudin-2, visualized in white; area 2, low occludin, high

claudin-2, visualized in cyan; area 3, high occludin, high claudin-2, visualized in magenta (Fig. S6). % occludin signal co-localized with claudin-2 was calculated as [100% * area 3 / (area 1 + area 3)], % claudin-2 signal not co-localized with occludin was calculated as [100% * area 2 / (area 2 + area 3)] for each image (2 sections each from 4 WT and 3 KO animals, 2 images per section).

For estimation of the PCT area covered by Claudin-2, images were recorded from regions predominantly containing PCT segments. Two intensity thresholds were defined within the total intensity range of 0 – 255: area 1 containing pixels with intensities > 115 to estimate specific Cldn2 signal and area 2 containing pixels with intensities > 30 to estimate total PT area. The ratio of [100% area 1 / (area 1 + area 2)] was calculated for each image (2 sections each from 4 WT and 3 KO animals, 3 images per section).

To determine claudin-2 redistribution in S3 segments, co-localization between ZO-1 and claudin-2 signals was defined as all pixels with intensities > 100 in both channels. Mean ZO-1 and claudin-2 intensities of these pixels were determined for each image (2 sections each from 4 WT and 3 KO animals, 2 to 3 images per section).

RNA-Seq

PT (~15 per sample) and DCT (~20 per sample) segments were isolated as described above. RNA was extracted using the Rneasy Plus Micro kit (Qiagen), following the manufactures instructions. RNA was sent to the University of Cologne sequencing facility for further processing. Quality control confirmed Rin^e values of $\geq$ 8.5 for all but one PT *Cldn10a* KO sample with a value of 6.0. Due to low amount of input material, pre-amplification using the Ovation RNA-Seq System V2 was performed. Total RNA was used for first strand cDNA synthesis, using both poly(T) and random primers, followed by second strand synthesis and isothermal strand-displacement amplification. For cDNA library preparation, the Illumina Nextera XT DNA sample preparation protocol was used, with 1 ng cDNA input. After validation (Agilent 4200 TapeStation) and quantification (Invitrogen Qubit System) all six transcriptome libraries were pooled. The pool was quantified using the Peqlab KAPA Library Quantification Kit and the Applied Biosystems 7900HT Sequence Detection and pooled on an Illumina NovaSeq6000 sequencing instrument run with PE100 read length (original data accession GSE167928).

Differential gene expression analysis and functional enrichment analysis

Mapped reads (STAR 2.5, default parameters) were assigned to genes using the summarizeOverlaps function of the GenomicRanges Bioconductor package with the

annotation from the GRCm38 mouse genome from NCBI resulting in tables of raw counts per gene for every sample.[32] Subsequent differential expression analysis was performed using Bioconductor software package DESeq2 v 1.24.0.[33] The DESeq2 method assesses differential expression by dispersion estimation and utilization of binomial generalized linear models.

For the DESeq2 analysis, low count transcripts were excluded i.e., only genes with at least 10 reads in at least 3 samples were used for analysis. Furthermore, the hidden and unwanted variations were removed with the statistical methods designed for RNA-Seq from the RUVSeq package in Bioconductor.[34]

When comparing reads within groups, one PCT *Cldn10a* KO sample turned out to be clearly contaminated by a more distal nephron segment (supplemental Fig. S7) and was therefore excluded from further analyses.

Functional enrichment analysis of differently expressed genes (Benjamin-Hochberg adjusted p-value < 0.1) was performed using g:Profiler.[35] The tool uses the Fisher's exact test to estimate significant overrepresentation of annotated terms in gene lists. Gene ontology annotation and a p-value threshold of 0.05 were used.

Electron microscopy of proximal tubule mitochondria

Kidneys were excised and transversely cut. Cuts for electron microscopy were fixed in 2.5% glutaraldehyde in 0.1 M sodium cacodylate buffer (pH 7.4) for about 3 hours at room temperature. Fixed tissues were stored in 0.5% glutaraldehyde in 0.1 M sodium cacodylate buffer (pH 7.4) at 4°C. Samples were further processed for transmission electron microscopy essentially as described previously.[36-38] Kidneys were washed in 0.2 M cacodylate buffer (pH 7.4) before vibratome sections were cut at 50 µm thickness. Kidney tissue blocks encompassing the renal cortex were dissected from vibratome sections, post-fixed in cacodylate buffer with 1% osmium tetroxide at room temperature for 1 h, rinsed in cacodylate buffer, dehydrated in a graded series of acetone including a 1% uranyl acetate stain at 70% acetone for 30 min and embedded in Durcupan araldite casting resin (Carl Roth, Karlsruhe, Germany). For structural orientation, semithin sections were cut at 1 µm thickness and stained with toluidine blue. Ultrathin sections (≈ 50 nm) were cut on an Ultracut II (Leica Microsystems, Wetzlar, Germany). Samples were imaged with a LEO-Zeiss EM 912 Omega TEM (Zeiss, Oberkochen, Germany) at 80 kV, and digital micrographs were obtained with a dual-speed 2K-on-axis CCD camera-based YAG scintillator (TRS-Tröndle, Moorenweis, Germany).

Imaging data were obtained from 4 WT and 4 *Cldn10a* KO mice. For morphometric analysis of proximal tubule mitochondria, imaging data (1-6 images per mouse from 3 WT and *3*

Cldn10a KO animals, amounting to 18-121 mitochondria per animal) were analyzed with ImageSP analysis Software (TRS-Tröndle, Moorenweis, Germany) with respect to their perimeter and cross-sectional area. Mitochondria were identified by their cristae. For statistical analysis, GraphPad Prism (USA) was used.

Electrophysiological analysis of claudin-2-transfected MDCK C7 cells

MDCK (Madin-Darby Canine Kidney) C7 cells, which stably expressed human claudin-2, were grown and handled as described before.[8] In brief, a clone with strong claudin-2 expression and without alteration in expression or localization of other TJ proteins was selected (clone 6 from [8]). Cells were grown to confluency on cell culture inserts and mounted in Ussing chambers 4 days post-seeding. Electrophysiological measurements were carried out as described in detail elsewhere.[7] Briefly, the bath solution on the basolateral side of the cell monolayer was iso-osmotically replaced with a modified solution, containing mannitol instead of NaCl. The resulting diffusion potential was used to calculate P_{Na}/P_{Cl}. Subsequently, the solution on the apical side was changed, thus replacing Na^+ by Ca^{2+}, Mg^{2+}, Sr^{2+}, or Ba^{2+}, respectively. The obtained bi-ionic potentials were used for calculation of relative cation permeabilities P_X/P_{Cl}.

Statistics

Unless otherwise stated (RNA-Seq, differential gene expression), data are presented as mean ± SEM and were tested (WT vs. KO) using two-sided Student's t-test. The threshold for statistical significance was set for p values <0.05.

RESULTS

Renal expression and localization of claudin-10a

RNA-Seq data confirmed the expression of *Cldn1*, *Cldn2*, *Cldn10a*, and *Cldn12* mRNA in PT from wild-type (WT) mice. In *Cldn10a* knockout (KO) mice, mRNA levels of *Cldn1*, *Cldn2*, and *Cldn12* were unaltered, *Cldn10a* mRNA was not detectable (Fig. 1A; supplementary Table S6a). Results for *Cldn2* were confirmed by quantitative PCR on isolated PT (Fig. S8). mRNA levels for claudins in DCT and in whole kidney extracts were unaltered by Cldn10a KO (Table S6a, b).

Western Blots on isolated PT demonstrated the presence of claudin-10 in WT, but its absence in *Cldn10a* KO tubules, confirming the successful deletion of *Cldn10a* as well as the absence of claudin-10b from proximal tubules (Fig. 1B).

Immunofluorescence staining of kidney sections confirmed localization of claudin-10 in WT PT TJs (Fig. 1C). Whereas TAL signals were unaltered by *Cldn10a* deletion, signals in PT were absent (Fig. 1C, D). Claudin-1 and claudin-12 were not detectable (not shown). These results confirm that the PT *Cldn10* isoform is claudin-10a, the TAL isoform is claudin-10b. Western Blot analyses of total kidney extracts from WT and *Cldn10a* KO mice showed decreased claudin-10 signal in *Cldn10a* KO mice. The remaining signal reflects the presence of claudin-10b, as the antibody does not discriminate between these two isoforms (Fig. S9).

Cldn10a has previously been found to be expressed only in kidney and uterus.[7] An additional quantitative PCR analysis of different intestinal segments indicated negligible amounts of *Cldn10a* in duodenum and complete absence in all other segments. Furthermore, the expression of *Cldn10b* was not affected by *Cldn10a* KO throughout the entire intestine (Fig. S8).

Phenotype of Cldn10a KO

Cldn10a KO animals were fertile and did not exhibit any overt macroscopic phenotypes or major alterations in clinical chemistry. Blood pH was unaltered (WT: pH 7.35 ± 0.003, n=11; KO: pH 7.36 ± 0.008, n=10), although, as depicted in Fig. 2, *Cldn10a* KO induced a urine alkalinization by approximately 0.5 pH units. Fractional Ca^{2+} and Mg^{2+} excretion was decreased and the latter resulted in mild hypermagnesemia. Serum calcium was not affected. Plasma urea concentration was slightly higher in KO.

Isolated PCT and TAL electrophysiology: Na^+, Cl^-, HCO_3^-

Proximal tubules were isolated and sorted into convoluted (PCT, late S1 and S2) and straight (PST, S3), depending on their morphology, as described in supplementary Fig. S5. Diffusion potential measurements (Fig. 3A) in WT showed a gradually decreasing anion over cation preference (positive dilution potential) from S1 to S2. S3 segments presented with a mild cation preference (negative dilution potential). Upon *Cldn10a* KO, permeabilities in S1, PCT and S2 converted into a substantial cation preference. In addition, S3 further increased its cation selectivity. For comparison, TAL segments from WT and KO animals were investigated, each resulting in strong cation selectivity (Fig. 3A), indicating that claudin-10a has no functional role in TAL, where claudin-10b is expressed.

PT reabsorbs HCO_3^- along the transcellular route.[39] Therefore, the paracellular anion permeability ought to distinguish between Cl^- and HCO_3^- and thus prevent a back-leakage of HCO_3^-. We therefore measured Cl^- vs. HCO_3^- diffusion potentials in isolated PT as well as TAL segments (Fig. 3B). In fact, positive diffusion potentials in WT PT showed preference of Cl^- over HCO_3^-, whereas in KO tubules diffusion potentials were around zero. In contrast to PT, both WT and *Cldn10a* KO TALs showed a substantial HCO_3^- over Cl^- preference (negative diffusion potentials, Fig. 3B), of course on the background of a very low total anion permeability. In summary, the results indicate that claudin-10a confers an anion permeability with a preference for Cl^- over HCO_3^- to PT TJs.

Claudin-2 redistribution in Cldn10a KO

After electrophysiological measurements, tubules were fixed and co-stained for claudin-10 and claudin-2 (Fig. 4A and supplemental Fig. S10). WT S1 segments showed claudin-10 in tight junctions and claudin-2 outside of tight junctions. In contrast, in *Cldn10a* KO tubules junctional claudin-2 and absence of claudin-10 were observed. In WT S2 and S3 segments, claudin-2 and claudin-10 co-localized. In KO, junctional claudin-2 staining was visible, but claudin-10 staining was absent. Western Blots and real-time PCR on isolated PCT, however, demonstrated, that the amount of *Cldn2* in KO PCT was unchanged compared to WT (Fig. 4B, Fig. S8). Together, these results suggested that claudin-2 redistributed in Cldn10a KO and that additional claudin-2 inserted into the TJ.

To demonstrate this redistribution, we performed detailed immunofluorescence studies in paraffin sections. Initially we intended to quantify claudin-2 colocalization with either occludin or ZO-1 as TJ markers. However, in PCT (S1 + S2) ZO-1 was not present and occludin staining was not junctional. For analysis we therefore made use of the specific staining pattern of occludin in vesicular structures outside the TJ of S1 segments. In WT PCT we observed a large amount of extra-junctional claudin-2 staining. To test whether this claudin-2 reservoir decreased upon *Cldn10a* KO, we evaluated the percentage of PCT area occupied by claudin-

2 in kidney sections. As shown in Fig. 4C, this percentage decreased, indicating either a decrease in total claudin-2 or an accumulation of claudin-2 in TJ strands. In WT S1 segments we further observed that occludin-positive vesicular structures strongly co-localized with claudin-2 staining. Quantification demonstrated that the percentage of occludin associated with claudin-2 decreased in *Cldn10a* KO and that the proportion of claudin-2 signal not associated with occludin in vesicles increased (Fig. 4D). In S3 segments, ZO-1 was present as a marker of the TJ. WT S3 segments showed clear junctional claudin-2, but claudin-2 signals further increased in *Cldn10a* KO (Fig. 4E).

From these findings, together with the results that neither RNA nor protein levels were altered, we conclude that claudin-2 in *Cldn10a* KO redistributes from intracellular compartments to the TJ.

Isolated PCT and TAL electrophysiology: Ca^{2+}, Mg^{2+}

As *Cldn10a* KO showed lower urinary Ca^{2+} and Mg^{2+} excretion, we investigated the permeability of *Cldn2* for the major cations in transfected MDCK C7 monolayers. The results are shown in Fig. 5A and demonstrate an increased permeability for Na^+, Ca^{2+} and Mg^{2+}.

This cation permeability, together with the observed redistribution of claudin-2 into the TJ upon *Cldn10a* KO implicated that the differences in diffusion potentials presented in Fig. 3 may be due to a decrease in P_{Cl}, an increase in P_{Na}, or a combination of both. To assess permeabilities independent from changes in P_{Cl} or P_{Na}, we carried out a second set of diffusion potential measurements, using solutions in which Cl^- was replaced by pyruvate, as we previously found claudin-10a to be impermeable to pyruvate.[7] The results for P_{Na}/P_{Pyr}, P_{Ca}/P_{Pyr} and P_{Mg}/P_{Pyr} are shown in Fig. 5B-D. In addition, we used the median P_{Na}/P_{Pyr} values to convert P_{Cl}/P_{Na} and P_{HCO3}/P_{Na} values calculated from the experiment shown in Fig. 3 into P_{Cl}/P_{Pyr} and P_{HCO3}/P_{Pyr} (Fig. 5E, F). The results show that *Cldn10a* KO reduced P_{Cl}/P_{pyr} in all PT segments by a similar amount. The increase in P_{Na}/P_{Pyr} was pronounced in S1 and PCT, moderate in S3, but failed to reach significance in S2. Both, P_{Ca}/P_{Pyr} and P_{Mg}/P_{Pyr} were increased in S1 and S3 segments. P_{HCO3}/P_{Pyr} was not affected by *Cldn10a* KO.

Compensatory alterations in para- and transcellular transport proteins

Western Blots on whole kidney extracts indicate a claudin-2 increase in *Cldn10a* KO compared to WT. The source of this additional claudin-2 remains unclear, however, claudin-2 is also expressed in other segments of the nephron, e.g., the descending thin limb of Henle's loop (Fig. S9). Thus, more distal claudin-2 up-regulation cannot be ruled out, as proximal tubular claudin-2 was unaltered.

The blots further revealed compensatory upregulation of NKCC2 (TAL), NCC and pNCC (DCT), as well as AQP2 and glycosylated AQP2 (CNT and CD) (Fig. 6A, B). Upregulation of NKCC2, as well as increased phosphorylation of NCC could also be demonstrated by immunofluorescence, whereas staining intensity for the PT transporters NaPi-IIa and NHE3 remained unaltered (Fig. 6C).

As the observed alterations were reminiscent of alterations induced by antidiuretic hormone (ADH), serum copeptin was measured as a surrogate marker for ADH. However, copeptin levels, as determined by ELISA, were not significantly different between WT (67.2 ± 17.9 pg/ml, n = 5) and *Cldn10a* KO mice (72.8 ± 23.8 pg/ml, n = 5).

Pharmacological treatment

The compensatory changes in transporter abundance and phosphorylation prompted us to try to unmask the respective functional changes by pharmacological interventions with tubular transport. We observed only minor differences between WT and KO for the treatment with acetazolamide (inhibition of carbonic anhydrase in PT, TAL, and CD), furosemide (inhibition of NKCC2 in TAL), and hydrochlorothiazide (inhibition of NCC in distal convoluted tubule). Urine analysis indicated that *Cldn10a* KO animals were in a compensatory state by the activation of transcellular Na^+ absorption and K^+ excretion, as well as Cl^- and HCO_3^- reabsorption (supplementary Tables S7a to S7d).

RNA sequencing analyses

To elucidate potential compensatory gene regulation in *Cldn10a* KO, PCT and DCT segments were micro-dissected from four WT and four *Cldn10a* KO mice and RNA was extracted to perform Illumina NovaSeq RNA-Seq analyses. In the PCT, 176 genes (102 up-regulated, 74 down-regulated) showed significant differential expression between genotypes (Fig. S11A). Functional enrichment analysis of these genes showed involvement in various processes of energy metabolism. Strongest enrichment was found for the following terms: small molecule-, organic acid-, carboxylic acid-, oxoacid-, fatty acid-, monocarboxylic acid-, lipid metabolic process overall indicating an increased energy demand of *Cldn10a* KO PCTs (Fig. 7A; supplemental Table S8; Fig. S11B). In DCT, no relevant changes between WT and KO were found (supplemental Fig. S11C).

PCT O_2 consumption and mitochondrial morphology

To substantiate the results from the RNA-Seq analysis, we determined O_2 consumption of isolated PCT suspended in a nutrient enriched solution (DMEM) as well as in a minimal solution. The difference in O_2 consumption between these two solutions was taken as a measure for nutrient-stimulated metabolism. This value was increased in *Cldn10a* KO compared to WT PCT (Fig. 7B).

Despite the differences in nutrient-stimulated metabolism, analysis of electron micrographs did not reveal any changes in mitochondrial perimeter or area (Fig. 7C, Fig. S12).

Fractional excretion of lithium

RNA-Seq data and O_2 consumption strongly suggest that the PT itself contributes substantially to the compensation of the paracellular *Cldn10a* KO. To assess the proximal tubular handling of salt and water we measured endogenous fractional excretion of lithium as a surrogate marker of PT function.[40, 41] Our data show no differences in this functional parameter (Fig. 2) although paracellular permeability for Li^+ increased in parallel to Na^+ (Fig. S5C).

DISCUSSION

Present results show that mouse PT epithelial cells express mRNA for *Cldn2* > *Cldn10a* = *Cldn12* > *Cldn1.* Furthermore, only the presence of Claudin-2 and -10 could be verified by immunohistology. No evidence was found for the previously postulated presence of claudin-17.[42]

Claudin-2 and claudin-10a are known to form paracellular channels, claudin-2 for inorganic cations and water (monovalent cations;[17,19] divalent cations;[18,43] water[8,44]), claudin-10a for anions.[6,7] Both paracellular channels act in parallel to facilitate paracellular cation and anion reabsorption, driven by the respective electrochemical gradients that build up upon the action of transcellular transport mechanisms.

Along the PT, clear opposing axial gradients of claudin-10a and -2 were found, starting from almost exclusive claudin-10a directly after the glomerulus to predominantly claudin-2 in the S3 segment. These gradients were paralleled by a transition from paracellular anion to cation preference along the PT, thereby confirming and complementing data from literature.[14-16] When simultaneously measuring both pore forming claudins via diffusion potential recordings in WT proximal tubules, the resulting selectivity was not very pronounced but it changed from anion selectivity in the early parts (PCT values comparable to[14]) to cation preference at the end of the proximal tubules (similar to[15,16]), with the turning point within the S2 segment. Similarly, transepithelial voltage and transepithelial resistance (supplementary Table S3) were in

accordance with data from the literature,[15,16] but unchanged by claudin-10a knockout. Only in S3 from KO did we observe a slightly more negative transepithelial voltage. However, data were measured under symmetric ion conditions and do not allow to draw conclusions on *in situ* driving forces. In previous studies, deficiency for the cation selective claudins led to anion-selectivity (claudin-2 deficiency: P_{Na}/P_{Cl} from 1.1 to 0.5; claudin-12 deficiency: P_{Na}/P_{Cl} from 1.25 to 0.67)[15,16]. Absence of claudin-10a from the proximal tubular tight junction resulted in more dramatic changes in selectivity with P_{Na}/P_{Cl} from ≤ 1 to 5, especially in the more proximal segments which have not been investigated by the previous studies. Bi-ionic Cl^-/HCO_3^- diffusion potentials revealed a similar Cl^- preference as previously reported[14] ($P_{Cl}/P_{HCO3} \approx 2$). This preference was lost in claudin-10a deficient PT at the expense of P_{Cl}.

Comparison of permeability values to the impermeant anion pyruvate revealed that *Cldn10a* KO increased P_{Na} and decreased P_{Cl}. The increase in P_{Na} was accompanied by an increase in P_{Ca} and P_{Mg}. (Fig. 5) which agrees with the permeability properties of claudin-2.[15,17,19,43] Differences along the axis might be attributed to other proximal tubular claudins, e.g., additional claudin-12 (see also Table S6a) and will be subject to future studies.

The observed loss of the paracellular anion permeability has physiological consequences for proximal tubular and entire renal electrolyte handling: about 60% of the glomerular filtrate is reabsorbed already along the PT. The most energy-efficient way to achieve this task is the combination of paracellular and transcellular routes.[45,46] In the early PT, Na^+-dependent, partially electrogenic co- and antiporters are driven by the basolateral Na^+/K^+-ATPase, generating a lumen negative transepithelial voltage. Cl^- concentration is increasing due to the preferred reabsorption of nutrients and HCO_3^-, and consecutively of water (Fig. 8).

Hence, in the early PT, Cl^- is reabsorbed along the paracellular pathway as long as the electrochemical gradient (lumen negative voltage and Cl^- concentration gradient) favours such a transport and as long as the TJs exhibit sufficient paracellular anion permeability.[47] The present data indicate that this Cl^- permeability is dependent on claudin-10a (Fig. 8A, upper part). In the late PT, luminal substrate concentrations become low and the lumen negative voltage source for Cl^- reabsorption by electrogenic Na^+ dependent cotransport fades. Instead, the lumen becomes even positive due to passive paracellular Cl^- diffusion along the still existing Cl^- gradient from the lumen to the basolateral side.[47]

In this late part of the PT, NaCl reabsorption is supported by the combination of Na^+/H^+ exchange and Cl^-/HCO_3^- exchange, where the exchanged anion finally recycles after protonation by non-ionic diffusion.[47] However, this transcellular mechanism comes with a higher energy expenditure.[19,46] Depending on the electrochemical gradients (lumen positive voltage and concentration gradient) and on the paracellular permeability, inorganic cations like

Na$^+$ and Ca^{2+} utilize the paracellular pathway, mainly supported by claudin-2 now increasingly present in the TJ (Fig 8A, lower part).

As depicted in Fig. 8B, an isolated defect in paracellular Cl$^-$ permeability in *Cldn10a* KO mice, together with the redistribution of claudin-2 into early PT TJs, i.e. gain in paracellular cation permeability, has the potential to impair overall PT transport. At least, a higher load of Cl$^-$ and H$_2$O would be delivered to the late PT, descending thin limb, and further downstream nephron segments (Fig. 8B) engaging this major part of the nephron with compensation.[48]

Accordingly, deletion of *Cldn10a* in mice did not induce any overt phenotype. Patients with isoform specific *CLDN10A* mutations are not known to date. Moreover, in patients suffering from HELIX syndrome, which is caused by mutations in the *CLDN10* gene, there is no obvious correlation between their symptoms and the underlying mutation affecting either solely *CLDN10B* or both, *CLDN10A* and *10B*.[26]

Similarly, deletion of *Cldn2* in mice has previously been shown to have only minor effects on water and electrolyte homeostasis and the authors were able to demonstrate that the kidney was able to compensate the loss of claudin-2 by transporting Na$^+$ along the less energy efficient transcellular pathway.[19]

Taken together the following conclusions are drawn from the present results:

1) The lack of claudin-10a in the PT is structurally, but not functionally compensated by redistribution of extra-junctional claudin-2 towards the TJ, similar to the translocation of Claudin-16/19 to Claudin-10b TJ in TAL.[49] This causes a switch from an anion preference (S1) or only slight cation preference (S3) of the paracellular pathway to a strongly cation preferring pathway (comparable in magnitude to the TAL).[50] As claudin-2 also conveys permeability to divalent cations,[18,43] this is most likely the reason for the observed hypermagnesemia and divalent cation retention in the *Cldn10a* KO mice. For HELIX syndrome patients this may mean that a mutation affecting both *CLDN10A* and *CLDN10B* may aggravate hypermagnesemia, a hallmark of this syndrome.

2) It has previously been postulated that claudin-10a conveys Cl$^-$ but not HCO$_3^-$ permeability to TJs.[42] The present data corroborate these findings: WT PTs present with a substantial Cl$^-$ over HCO$_3^-$ permeability. In terms of PT physiology, this is plausible, as it prevents HCO$_3^-$ from back leaking into the tubular lumen. This HCO$_3^-$ tightness is preserved in *Cldn10a* KO.

3) If Cl$^-$ cannot be transported along the paracellular pathway (usually ~70%),[51] it will have to take the transcellular route. If this transcellular Cl$^-$ transport occurred in the PT, this could be partially at the expense of HCO$_3^-$ (Fig. 8). The observed more alkaline urine in *Cldn10a* KO (about 0.5 pH units compared to WT) in untreated as well as acetazolamide or furosemide treated animals, favours this hypothesis. Yet, acetazolamide did not aggravate urine

alkalinization. As carbonic anhydrase inhibition interferes with any renal acid-base transport and acid-base transport occurs in PT, TAL, CNT, DCT, and CD, the interpretation of these observations remains speculative. They may indicate (i) that the PT is already able to neutralize tubular pH, (ii) that compensation occurs further downstream, or (iii) that the alkalinization itself is caused by downstream compensatory mechanisms.[52,for rev.53]

RNA-Seq data not necessarily have to mirror expression. Also in this study, up-regulation of NCC is found on protein but not on RNA level. This is not too surprising, as protein levels may also be affected by, e.g., alterations in protein degradation that would not be reflected by RNA levels.[54] Taken together, our data revealed clear indications for compensation of the PT defect in NaCl reabsorption.[48] Total amount (NKCC2, NCC, AQP2) as well as phosphorylated (pNCC) or glycosylated (AQP2) amount of several solute transporters were increased. Increased TAL and DCT NaCl transport contribute to the mild phenotype. Fractional excretion of K^+ or increased K^+/crea ratio indicates collecting duct principal cell activation of luminal Na^+ absorption coupled to the corresponding K^+ excretion. The same was observed for Cl^- due to distal HCO_3^- rescue.[55] Furosemide treatment revealed two very interesting observations: i) during furosemide treatment, creatinine clearance as a surrogate marker for GFR was reduced, probably due to the developing volume depletion in KO in the absence of TAL compensation.[56] ii) urine acidification, usually occurring under furosemide,[57] is lacking in KO and speaks in favour of a substantial change in TAL and collecting duct H^+ transport.

We speculate that treatment with the different drugs only one at a time prevented the observation of the full-blown effect of the knockout and strongly points towards the impressive compensatory capacity of any functional segment along the nephron.[48]

4) Finally, similar to *Cldn2* KO mice,[19] compensation of claudin-10a loss appears to change renal metabolic capacity, as PT RNA-Seq data indicate an increased expression of proteins involved in energy metabolism and respirometry showed higher nutrient stimulated O_2 consumption. This could be a result of a shift towards an intensified transcellular Na^+ and Cl^- transport already in late PT.[58]

In conclusion, claudin-10a is responsible for paracellular anion permeability of PT. In *Cldn10a* KO, claudin-2 redistributes to the TJ and is hypothesized to cause hyper-reabsorption of Mg^{2+} and Ca^{2+}.

The lack of paracellular Cl^- transport is compensated already in PT by the energetically costly transcellular transport, thus reducing HCO_3^- reabsorption and causing activation of metabolic pathways.

In humans, *CLDN10* mutations affecting *CLDN10A* and *CLDN10B*, rather than only *CLDN10B*, may aggravate hypermagnesemia observed in HELIX syndrome and make the patients more susceptible to ischemia, volume depletion, or acid-base disturbances.

Author Contributions

TB, NH, JH, SM, MB, DG contributed to conception and design of the study. TB, NH, JA, AF, SMK, YL, LM, CQ, MS, DGS, UW, MM, SS, MAB, CM, NK, KM, ON, MRS, MB, DG were involved in data acquisition and analysis. TB, NH, YL, DM, ON, SS, JH, MB, DG contributed to interpretation of data and provided supervision and technical support. DG and MB drafted the manuscript. All authors contributed to revision of the final version of the manuscript and approved the final submitted version.

Disclosures

Nothing to disclose

Supplemental material – Table of Contents

REFERENCES

1. Furuse M, Fujita K, Hiiragi T, Fujimoto K, Tsukita S: Claudin-1 and -2: novel integral membrane proteins localizing at tight junctions with no sequence similarity to occludin. *J Cell Biol* 141: 1539–1550, 1998

2. Günzel D, Yu AS: Claudins and the modulation of tight junction permeability. *Physiol Rev* 93: 525–569, 2013

3. Krug SM, Schulzke JD, Fromm M: Tight junction, selective permeability, and related diseases. *Semin Cell Devel Biol* 36: 166–176, 2014

4. Fromm M, Piontek J, Rosenthal R, Günzel D, Krug SM: Tight junctions of the proximal tubule and their channel proteins. Pflügers Arch 469: 877–887, 2017

5. Meoli L, Günzel D: Channel functions of claudins in the organization of biological systems. *BBA - Biomembr* 1862: 183344, 2020

6. Van Itallie CM, Rogan S, Yu AS, Seminario-Vidal L, Holmes J, Anderson JM: Two splice variants of claudin-10 in the kidney create paracellular pores with different ion selectivities. *Am J Physiol Renal Physiol* 291: F1288–F1299, 2006

7. Günzel D, Stuiver M, Kausalya PJ, Haisch L, Krug SM, Rosenthal R, et al.: Claudin-10 exists in six alternatively spliced isoforms which exhibit distinct localization and function. *J Cell Sci* 122: 1507–1517, 2009

8. Rosenthal R, Milatz S, Krug SM, Oelrich B, Schulzke JD, Amasheh S, et al.: Claudin-2, a component of the tight junction, forms a paracellular water channel. *J Cell Sci* 123: 1913–1921, 2010

9. Kiuchi-Saishin Y, Gotoh S, Furuse M, Takasuga A, Tano Y, Tsukita S: Differential expression patterns of claudins, tight junction membrane proteins, in mouse nephron segments. *J Am Soc Nephrol* 13: 875–886, 2002

10. Kirk A, Campbell S, Bass P, Mason J, Collins J: Differential expression of claudin tight junction proteins in the human cortical nephron. *Nephrol Dial Transplant* 25: 2107–2119, 2010

11. Lee JW, Chou CL, Knepper MA: Deep Sequencing in Microdissected Renal Tubules Identifies Nephron Segment-Specific Transcriptomes. *J Am Soc Nephrol* 26: 2669–2677, 2015

12. Breiderhoff T, Himmerkus N, Stuiver M, Mutig K, Will C, Meij IC, et al.: Deletion of claudin-10 (Cldn10) in the thick ascending limb impairs paracellular sodium permeability and leads to hypermagnesemia and nephrocalcinosis. *Proc Natl Acad Sci USA* 109: 14241–14246, 2012

13. Plain A, Wulfmeyer VC, Milatz S, Klietz A, Hou J, Bleich M, et al.: Corticomedullary difference in the effects of dietary Ca^{2+} on tight junction properties in thick ascending limbs of Henle's loop. Pflügers Arch 468: 293–303, 2016

14. Abuazza G, Becker A, Williams SS, Chakravarty S, Truong HT, Lin F, et al.: Claudins 6, 9, 13 are developmentally expressed renal tight junction proteins. *Am J Physiol Renal Physiol* 291: F1132–F1141, 2006

15. Muto S, Hata M, Taniguchi J, Tsuruoka S, Moriwaki K, Saitou M, et al.: Claudin-2-deficient mice are defective in the leaky and cation-selective paracellular permeability properties of renal proximal tubules. *Proc Natl Acad Sci USA* 107: 8011–8016, 2010

16. Plain A, Pan W, O'Neill D, Ure M, Beggs MR, Farhan M, et al.: Claudin-12 knockout mice demonstrate reduced proximal tubule calcium permeability. *Int J Mol Sci* 21: 2074, 2020

17. Amasheh S, Meiri N, Gitter AH, Schöneberg T, Mankertz J, Schulzke JD, et al.: Claudin-2 expression induces cation-selective channels in tight junctions of epithelial cells. *J Cell Sci* 115: 4969–4976, 2002

18. Fujita H, Sugimoto K, Inatomi S, Maeda T, Osanai M, Uchiyama Y, et al.: Tight junction proteins claudin-2 and -12 are critical for vitamin D-dependent Ca^{2+} absorption between enterocytes. *Mol Biol Cell* 19: 1912–1921, 2008

19. Pei L, Solis G, Nguyen MT, Kamat N, Magenheimer L, Zhuo M et al.: Paracellular epithelial sodium transport maximizes energy efficiency in the kidney. *J Clin Invest* 126: 2509–2518, 2016

20. Klar J, Piontek J, Milatz S, Tariq M, Jameel M, Breiderhoff T, et al. Altered paracellular cation permeability due to a rare CLDN10B variant causes anhidrosis and kidney damage. *Plos Genet* 13: e1006897, 2017

21. Bongers EMHF, Shelton LM, Milatz S, Verkaart S, Bech AP, Schoots J, et al.: A novel hypokalemic-alkalotic salt-losing tubulopathy in patients with CLDN10 mutations. *J Am Soc Nephrol* 28: 3118–3128, 2017

22. Hadj-Rabia S, Brideau G, Al-Sarraj Y, Maroun RC, Figueres ML, Leclerc-Mercier S:, Multiplex epithelium dysfunction due to CLDN10 mutation: the HELIX syndrome, *Genet Med* 20: 190–201, 2018

23. Meyers N, Nelson-Williams C, Malaga-Dieguez L, Kaufmann H, Loring E, Knight J: Hypokalemia associated with a claudin 10 mutation: a case report. *Am J Kidney Dis* 73: 425–428, 2019

24. Alzahrani AS, Hussein M, Alswailem M, Mouna A, Albalawi L, Moria Y, Jabbar MA, Shi Y, Günzel D, Dasouki M. A novel claudin-10 mutation with a unique mechanism in two unrelated families with HELIX syndrome. *Kidney Int* 100: 415-429, 2021

25 Sewerin S, Piontek J, Schönauer R, Grunewald S, Rauch A, Neuber S, Bergmann C, Günzel D, Halbritter J. Defective claudin-10 causes a novel variation of HELIX syndrome through compromised tight junction strand assembly. *Genes & Dis*. (in press)

26. Milatz S: A novel claudinopathy based on claudin-10 mutations. *Int J Mol Sci* 20: 5396, 2019

27. Gong Y, Renigunta V, Himmerkus N, Zhang J, Renigunta A, Bleich M et al.: Claudin-14 regulates renal Ca^{++} transport in response to CaSR signalling via a novel microRNA pathway. *EMBO J* 31: 1999–2012, 2012

28. Hou J, Renigunta V, Nie M, Sunq A, Himmerkus N, Quintanova C et al.: Phosphorylated claudin-16 interacts with Trpv5 and regulates transcellular calcium transport in the kidney. *Proc Natl Acad Sci USA* 116: 19176–19186, 2019

29. Pohl M, Kaminski H, Castrop H, Bader M, Himmerkus N, Bleich M, et al.: Intrarenal renin angiotensin system revisited: role of megalin-dependent endocytosis along the proximal nephron. *J Biol Chem* 285: 41935–41946, 2010

30. Lee H-G, Stumpp M, Yan J-J, Tseng Y-C, Heinzel S, Hu MY-A. Tipping points of gastric pH regulation and energetics in the sea urchin larva exposed to CO_2 -induced seawater acidification. *Comp Biochem Physiol A Mol Integr Physiol* 234: 87–97, 2019.

31. Greger R: Cation selectivity of the isolated perfused cortical thick ascending limb of Henle's loop of rabbit kidney. *Pflügers Arch* 390: 30–37, 1981

32. Lawrence M, Huber W, Pagès H, Aboyoun P, Carlson M, Gentleman R, et al.: Software for Computing and Annotating Genomic Ranges. *PLoS Comput Biol* 9: e1003118, 2013

33. Love MI, Huber W, Anders S: Moderated estimation of fold change and dispersion for RNA-seq data with DESeq2. *Genome Biol* 15: 550, 2014

34. Risso D, Ngai, J, Speed T, et al.: Normalization of RNA-seq data using factor analysis of control genes or samples. *Nat Biotechnol* 32: 896–902, 2014

35. Raudvere U, Kolberg L, Kuzmin I, Arak T, Adler P, Peterson H, et al.: g:Profiler: a web server for functional enrichment analysis and conversions of gene lists (2019 update). *Nucleic Acids Res* 47: 191–198, 2019

36. Blosa M, Sonntag M, Brückner G, Jäger C, Seeger G, Matthews RT, Rübsamen R, Arendt T, Morawski M. Unique features of extracellular matrix in the mouse medial nucleus of trapezoid body--implications for physiological functions. Neurosci 228: 215-234, 2013

37. Blosa M, Sonntag M, Jäger C, Weigel S, Seeger J, Frischknecht R, Seidenbecher CI, Matthews RT, Arendt T, Rübsamen R, Morawski M. The extracellular matrix molecule brevican is an integral component of the machinery mediating fast synaptic transmission at the calyx of Held. J Physiol 593: 4341-4360, 2015

38. Köppen J, Schulze A, Machner L, Wermann M, Eichentopf R, Guthardt M, Hähnel A, Klehm J, Kriegeskorte MC, Hartlage-Rübsamen M, Morawski M, von Hörsten S, Demuth HU, Roßner S, Schilling S. Amyloid-Beta Peptides Trigger Aggregation of Alpha-Synuclein In Vitro. Molecules 25: 580, 2020

39. Frömter E, Rumrich G, Ullrich KJ: Phenomenologic description of Na^+, Cl^- and HCO_3^- absorption from proximal tubules of the rat kidney. Pflügers Arch 343: 189–220, 1973

40. Folkerd E, Singer DR, Cappuccio FP, Markandu ND, Sampson B, MacGregor GA. Clearance of endogenous lithium in humans: altered dietary salt intake and comparison with exogenous lithium clearance. Am J Physiol. 268: F718-22, 1995

41. Zhuo JL, Li XC. Proximal nephron. Compr Physiol. 3: 1079-1123. 2013

42. Krug SM, Günzel D, Conrad MP, Rosenthal R, Fromm A, Amasheh S, et al. Claudin-17 forms tight junction channels with distinct anion selectivity. *Cell Mol Life Sci* 69: 2765–2778, 2012

43. Curry JN, Saurette M, Askari M, Pei L, Filla MB, Beggs MR, et al.: Claudin-2 deficiency associates with hypercalciuria in mice and human kidney stone disease. *J Clin Invest* 130: 1948–1960, 2020

44. Schnermann J, Huang Y, Mizel D: Fluid reabsorption in proximal convoluted tubules of mice with gene deletions of claudin-2 and/or aquaporin1. Am J Physiol Ren Physiol 305 F1352–F1364, 2013

45. García NH, Ramsey CR, Knox FG. Understanding the role of paracellular transport in the proximal tubule. News Physiol Sci 13: 38–43, 1998

46. Yu ASL. Paracellular transport and energy utilization in the renal tubule. Curr Opin Nephrol Hypertens 26: 398–404, 2017

47. Aronson PS, Giebisch G: Mechanisms of chloride transport in the proximal tubule *Am J Physiol Renal Physiol* 273: F179–F192, 1997

48. Schnermann J. Sodium transport deficiency and sodium balance in gene-targeted mice. Acta Physiol Scand 173: 59–66, 2001

49. Breiderhoff T, Himmerkus N, Drewell H, Plain A, Günzel D, Mutig K, et al. Deletion of claudin-10 rescues claudin-16-deficient mice from hypomagnesmia and hypercalciuria. Kidney Int. 93: 580–588, 2018

50. Milatz S, Himmerkus N, Wulfmeyer VC, Drewell H, Mutig K, Hou J, Breiderhoff T, et al. Mosaic expression of claudins in thick ascending limbs of Henle results in spatial separation of paracellular Na^+ and Mg^{2+} transport. Proc Natl Acad Sci USA 114: E219–E227, 2017

51. Weinstein AM, Weinbaum S, Duan Y, Du Z, Yan Q, Wang T. Flow-dependent transport in a mathematical model of rat proximal tubule. Am J Physiol Renal Physiol 292: F1164–F1181, 2007

52. Skelton LA, Boron WF, Zhou Y. Acid-base transport by the renal proximal tubule. J Nephrol 23 Suppl 16: S4–18, 2010

53. Kurtz I. Molecular mechanisms and regulation of urinary acidification. Compr Physiol 4: 1737–1774, 2014

54. Koussounadis A, Langdon SP, Um IH, Harrison DJ, Smith VA. Relationship between differentially expressed mRNA and mRNA-protein correlations in a xenograft model system. Sci Rep 5: 10775, 2015

55. Soleimani M. The multiple roles of pendrin in the kidney. Nephrol Dial Transplant 30: 1257–1266, 2015

56. Christensen S, Petersen JS. Effects of furosemide on renal haemodynamics and proximal tubular sodium reabsorption in conscious rats. Br J Pharmacol 95: 353–360, 1988

57. de Bruijn PI, Larsen CK, Frische S, Himmerkus N, Praetorius HA, Bleich M, et al. Furosemide-induced urinary acidification is caused by pronounced H^+ secretion in the thick ascending limb. Am J Physiol Renal Physiol 309: F146–F153, 2015

58. Dickman KG, Mandel LJ. Relationship between HCO_3^- transport and oxidative metabolism in rabbit proximal tubule. Am J Physiol 263: F342–F351, 1992

Figures
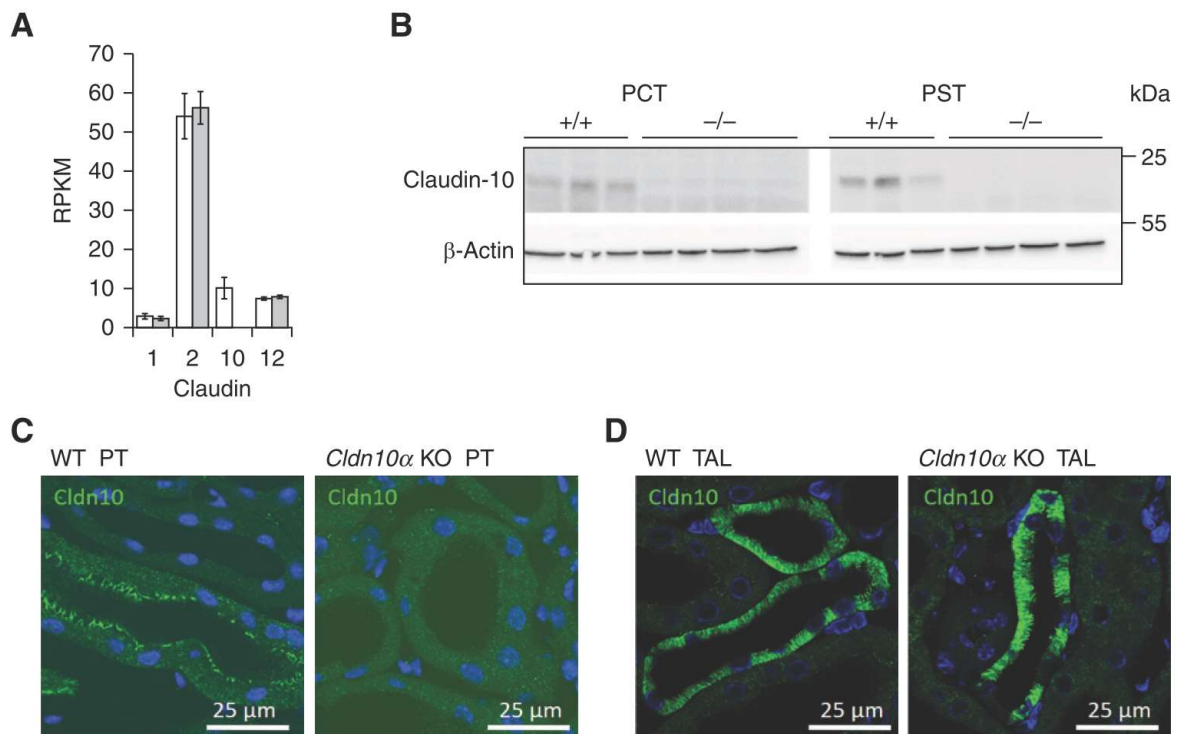
**Fig. 1: Expression of claudins in WT and *Cldn10a* KO proximal tubules.**

A Reads per kilobase of transcript, per million mapped reads (RPKM) for isolated WT (white) and KO (grey) proximal convoluted tubule segments (RNA-Seq data, means ± SEM, n = 4 WT and 3 KO mice).

B Western Blot from isolated proximal convoluted tubules (PCT) and isolated proximal straight tubules (PST/S3). Claudin-10 was present in tubules from wildtype mice (WT) but absent in knockout mouse (-/-) kidney proximal tubules.

C Immunostaining of claudin-10 in cortical kidney sections. Junctional claudin-10 signals (green) were visible in PT from WT animals (left), but absent in *Cldn10a* KO animals (right).

D In contrast, claudin-10 staining in TAL was unaffected by *Cldn10a* KO.

Blue, DAPI.
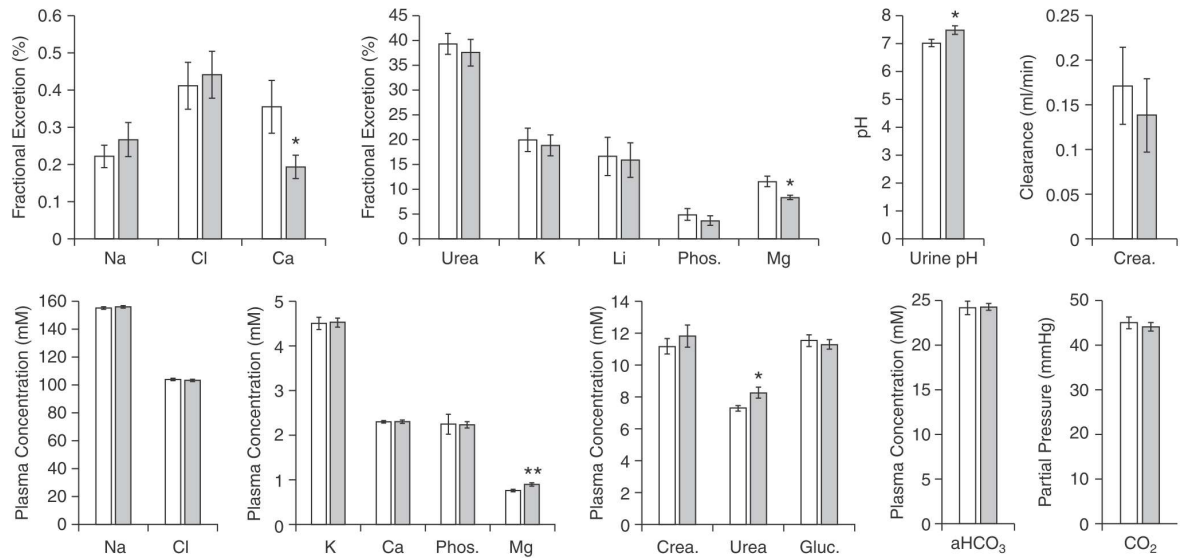
Fig. 2: Electrolytes and renal function parameters in WT (white) and *Cldn10a* KO (grey).

Upper panel: Fractional excretions of Na^+, Cl^-, Ca^{2+}, urea, K^+, Li^+, phosphate (Phos) and Mg^{2+}, as well as urine pH, and creatinine clearance as a measure of GFR. Fractional Ca^{2+} and Mg^{2+} excretion were reduced in *Cldn10a* KO animals. (* $p<0.05$; ** $p < 0.01$; n = 11 to 14)

Lower panel: Plasma concentrations of Na^+, Cl^-, K^+, Ca^{2+}, phosphate (Phos), Mg^{2+}, creatinine (Crea), urea, glucose (Gluc.), and bicarbonate ($aHCO_3^-$) at the respective CO_2 partial pressure (CO_2). Plasma Mg^{2+} and urea were elevated in *Cldn10a* KO animals. (* $p<0.05$; n = 14 to 15). The increase in plasma Mg^{2+} corresponded to the decrease in fractional Mg^{2+} excretion.
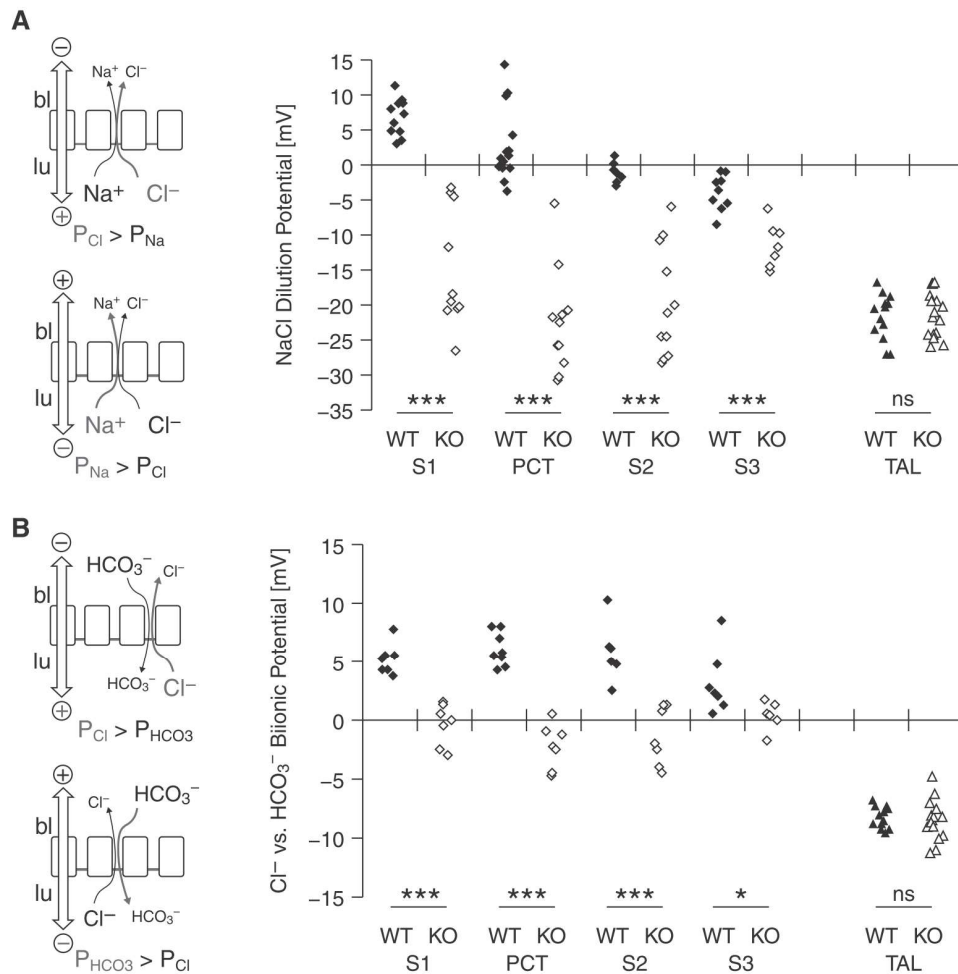
Fig. 3: Dilution and biionic potential measurements.

Dilution and biionic potentials were measured in isolated nephron segments (diamonds, proximal tubule: S1, PCT, S2, PST/S3 as defined in supplemental Fig. S2; triangles, thick ascending limb (TAL), for comparison). Black symbols, WT; open symbols, *Cldn10a* KO. n = 7 to 17, as described in the text; ns, not significant; *, $p<0.05$; ***, $p<<0.001$.

A Dilution potential. Measurements of transepithelial potential differences before and after switching the basolateral (bl) Na^+ and Cl^- concentrations from 145 mM and 149.8 mM to 30 mM and 39.8 mM, respectively. The luminal (lu) NaCl concentration remained unchanged. Lumen positive potentials indicate anion preference, negative potentials cation preference (see insets). In WT proximal tubule, there was a gradient from anion preference in S1 to moderate cation preference in PST/S3 segments. In *Cldn10a* KO, all proximal tubule segments showed pronounced cation preference. In TAL, cation preference was unaffected by *Cldn10a* KO.

B Biionic potential. Measurements of transepithelial potential differences under the condition of opposing Cl^- vs. HCO_3^- concentration gradients across the epithelium. After reverting to the original high Cl^- peritubular solution following the dilution potential measurements shown in (A), this solution was consecutively switched to low (9.8 mM) Cl^- and high (140 mM) HCO_3^-, with

Na$^+$ remaining symmetrically at 145 mM on both sides, to determine the Cl$^-$ vs. HCO$_3^-$ preference. Here, lumen positive potentials indicate Cl$^-$ over HCO$_3^-$ preference, negative potentials HCO$_3^-$ over Cl$^-$ preference (see inset). All WT proximal tubule segments preferred Cl$^-$ over HCO$_3^-$. This preference was lost in *Cldn10a* KO proximal tubules. In contrast, WT and *Cldn10a* KO TAL, though displaying low anion permeability, equally preferred HCO$_3^-$ over Cl$^-$.
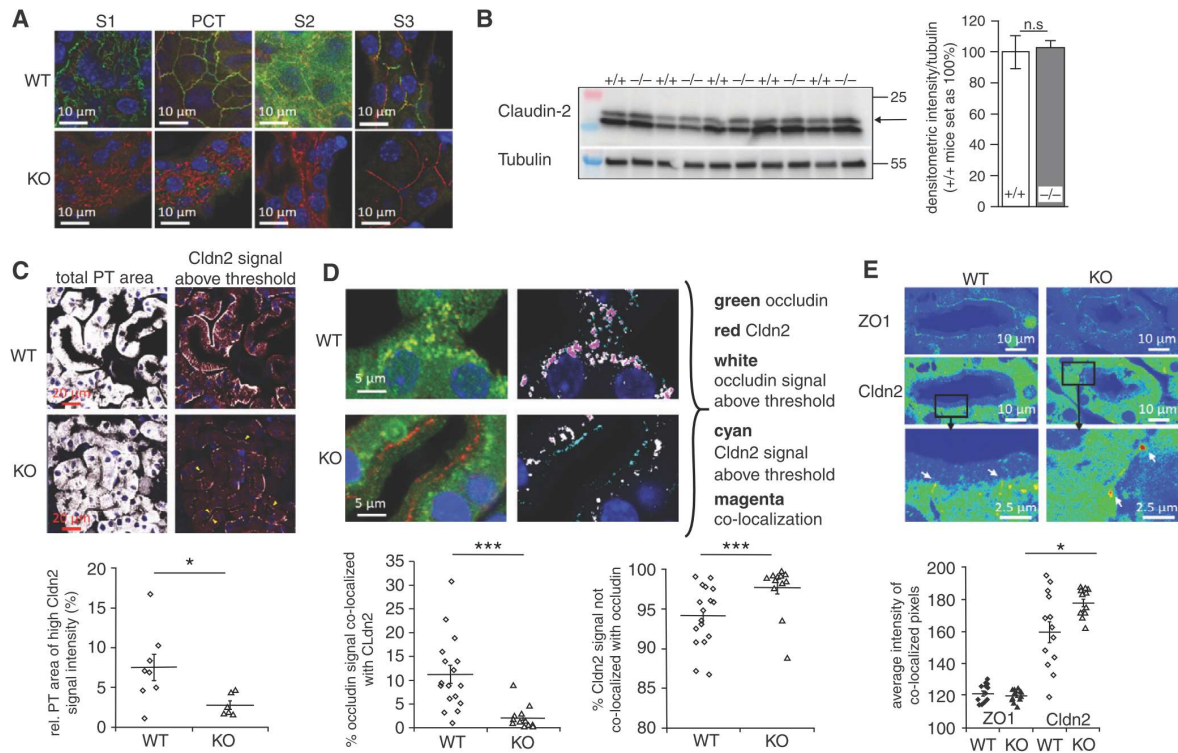
Fig. 4: Claudin-2 redistribution in *Cldn10a* KO.

A Co-immunostaining of claudin-10 (green) and claudin-2 (red) of isolated segments of the proximal tubule from S1 over PCT and S2 to PST/S3, as defined in supplemental Fig. S2. In WT, claudin-10 dominated the tight junction in the early segments. Further downstream, the junctions showed alternating staining of claudin-10 and -2 with the highest expression of claudin-2 in PST/S3. In *Cldn10a* KO, claudin-2 staining was found in the tight junctions all along the proximal tubule. Obviously, the absence of claudin-10a paved the way for claudin-2 incorporation into the tight junction. Blue, DAPI.

B Western Blot and densitometric evaluation of signals from PCT isolated from 5 WT and 5 *Cldn10a* KO kidneys demonstrate that PCT claudin-2 signals were unaltered in *Cldn10a* KO. Signal intensities are shown relative to the tubulin loading control signal and WT was set to 100%.

C Quantification of claudin-2 immunostaining in WT and *Cldn10a* KO by threshold analysis. The area of intensity above threshold was divided by the total area covered by proximal tubules. WT showed more claudin-2 positive pixels above threshold; the signal, however, was located mainly outside the tight junction and basolaterally. In contrast, claudin-2 in *Cldn10a* KO showed clear, almost exclusive and focused tight junction staining at the expense of total area above threshold. Below: Quantification, (n = 8 section (24 images) from 4 WT mice and 6 sections (18 images) from 3 KO mice; *, p<0.05)

D Co-immunostaining of claudin-2 (red) and occludin (green) in WT and *Cldn10a* KO S1 segments. Visualization of co-localization by threshold analysis. In WT proximal tubule, occludin and claudin-2 appeared together and above threshold outside the tight junction. In *Cldn10a* KO, claudin-2 segregated into the tight junction and dropped below threshold in the area where occludin remained above threshold. Below: Quantification of co-localization and segregation. (n = 17 images from 4 WT animals and 14 images from 3 KO mice; ***, $p < 0.001$)

E Co-immunostaining of ZO-1 (upper panels, rainbow palette, TJ = green line) and claudin-2 (lower panels, rainbow palette) in WT and *Cldn10a* KO S3 segments. High claudin-2 intensities (red dots in enlarged subsets) were only visible in *Cldn10a* KO sections. Below: Evaluation of co-localization was carried out by threshold analysis. ZO-1 intensities in ZO-1 co-localized pixels were not significantly different between WT and *Cldn10a* KO, whereas claudin-2 intensities in these pixels were higher in *Cldn10a* KO compared to WT. (n = 14 images from 4 WT animals and 13 images from 3 KO mice; *, $p < 0.05$).
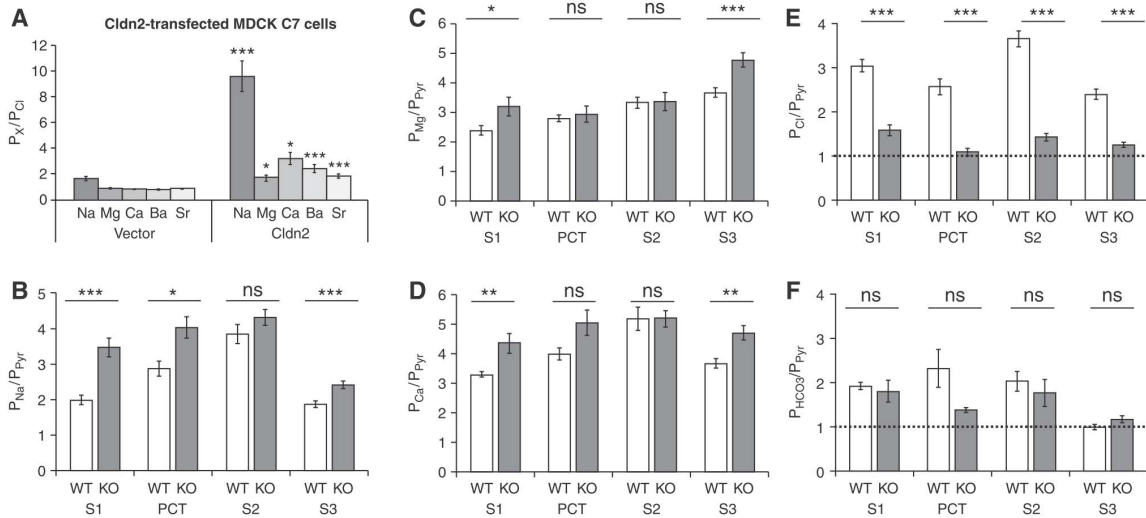
Fig. 5: Ion permeability ratios for claudin-2 in the expression system and along the proximal tubule segments of WT and *Cldn10a* KO.

A MDCK C7 cells transfected with claudin-2 showed increases in cation/Cl⁻ permeability ratio for Na⁺ and divalent cations, compared to vector transfected cells. **B-F** Individual permeability ratios for Na⁺, Mg²⁺, Ca²⁺, Cl⁻, and HCO₃⁻ with reference to the low permeant anion pyruvate. Permeability ratios are shown along the proximal tubule from S1 over PCT and S2 to PST/S3 (as defined in supplemental Fig. S5) for WT (white) and *Cldn10a* KO (grey). *Cldn10a* KO led to a sharp decrease in P_{Cl} in all segments. In addition, the permeability for all cations increased in S1 and S3 segments and for Na⁺ also in S2. The permeability for HCO₃⁻ was not affected by *Cldn10a* KO and remained as low as the permeability for pyruvate. (n = 15-20; *, p<0.05; **, p<0.01); ***, p<0.001)
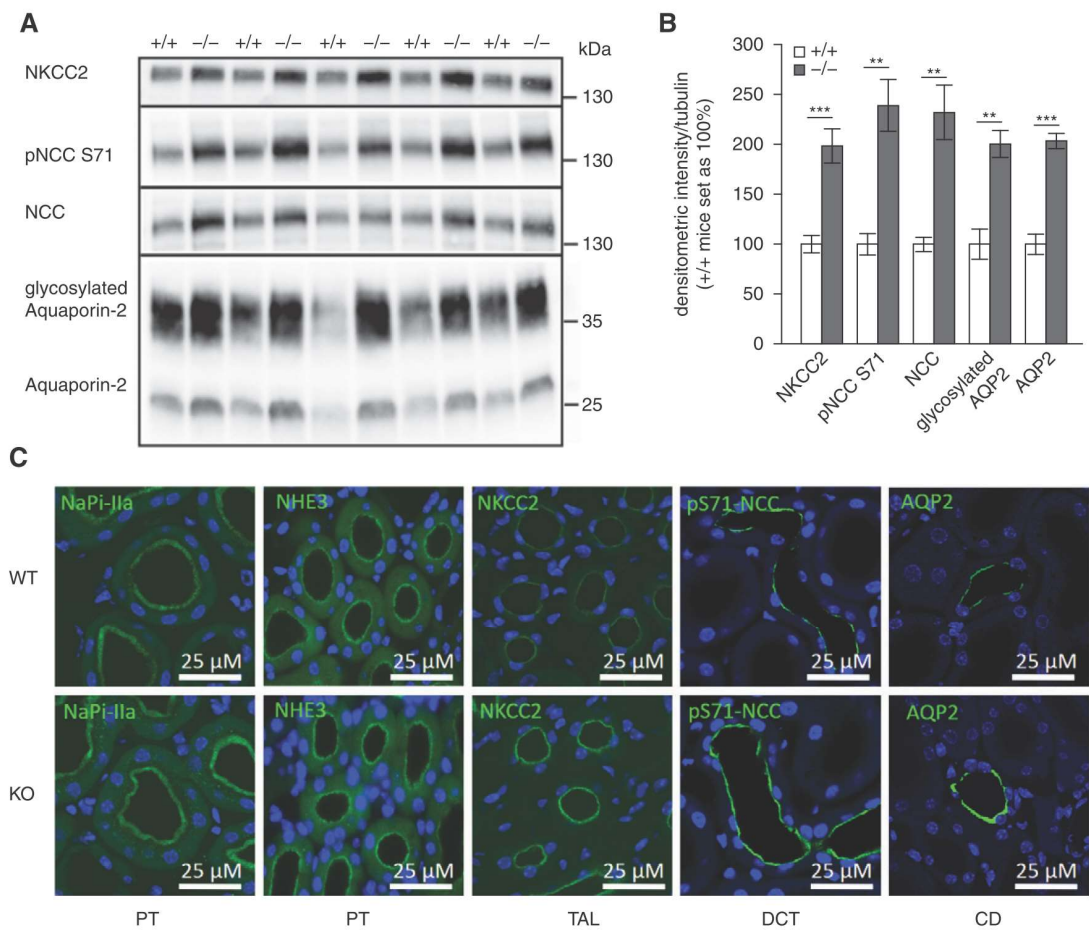
Fig. 6: Effect of *Cldn10a* KO on ion transport proteins downstream the proximal tubule.

Western Blots (**A**) and their densitometric evaluation (**B**) as well as immunofluorescence staining (**C**) demonstrated that signals for the proximal convoluted tubular (PCT) transport proteins Na$^+$-dependent phosphate transporter NaPi-IIa and Na$^+$/H$^+$ exchanger 3 (NHE3) were not affected by *Cldn10a* KO. In contrast, compared to WT, signals for *Cldn10a* KO total Na/K/2Cl symport (NKCC2; thick ascending limb, TAL), total and phosphorylated (S71) Na/Cl symport (NCC; distal convoluted tubule, DCT), and water channel aquaporin-2 (AQP2; collecting duct, CD) were increased (*, p < 0.05).
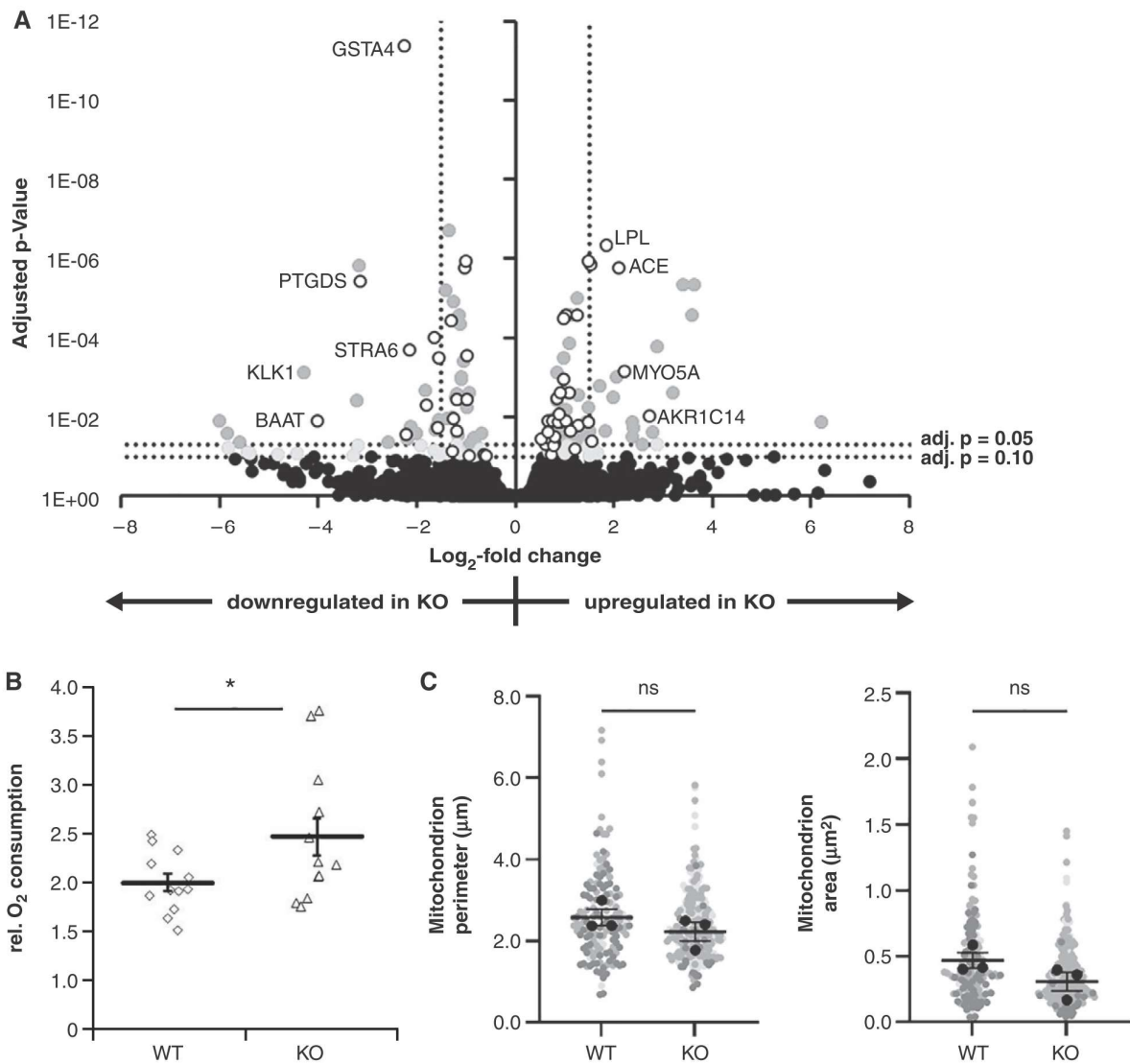
Fig. 7: Proximal tubule RNA-Seq analysis.

A Plot of $\log_2$-fold change between WT and *Cldn10a* KO PCT samples against the adjusted p-values. Dotted lines denote p = 0.05, p = 0.10 and $|\log_2$-fold change$|$ = 1.5. Value for Cldn10 is not shown as counts in *Cldn10a* KO samples were 0 (cf. Fig. 1).

Genes with significantly altered expression levels are marked in grey. Open circles mark genes related to fatty acid and lipid metabolic processes. Selected genes are labelled:

ACE, angiotensin I converting enzyme (peptidyl-dipeptidase A) 1 (ENSMUSG00000020681)
LPL, lipoprotein lipase (ENSMUSG00000015568)
AKR1C14, aldo-keto reductase family 1, member C14 (ENSMUSG00000033715)
MYO5A, myosin VA (ENSMUSG00000034593)
GSTA4, glutathione S-transferase, alpha 4 (ENSMUSG00000032348)
KLK1, kallikrein 1 (ENSMUSG00000063903)
PTGDS, prostaglandin D2 synthase (brain) (ENSMUSG00000015090)

STRA6, stimulated by retinoic acid gene 6 (ENSMUSG00000032327)

BAAT, bile acid-Coenzyme A: amino acid N-acyltransferase (ENSMUSG00000039653)

B Nutrient stimulated oxygen consumption (rel. O_2 consumption) of isolated proximal tubule segments (PCT) in WT and *Cldn10a* KO. Metabolism (%O_2 consumption/h/tubule) was compared between low and high nutrient solutions. *Cldn10a* KO tubules showed a higher increase in oxygen consumption in the presence of high nutrient concentrations compared to WT, indicating higher metabolic capacity. (n = 12 WT, 12 KO; *, $p<0.05$)

C Perimeters and cross-sectional areas of individual mitochondria (grey bullets) were not significantly different between WT and *Cldn10a* KO mice. Black bullets: means of individual mice. Two-tailed t-tests; ns, not significant; mean of means ± SEM; n (mice) = 3 (WT)/ 3 (KO); n (mitochondria per mouse) = 18-121; n (images per mouse) = 1-6.
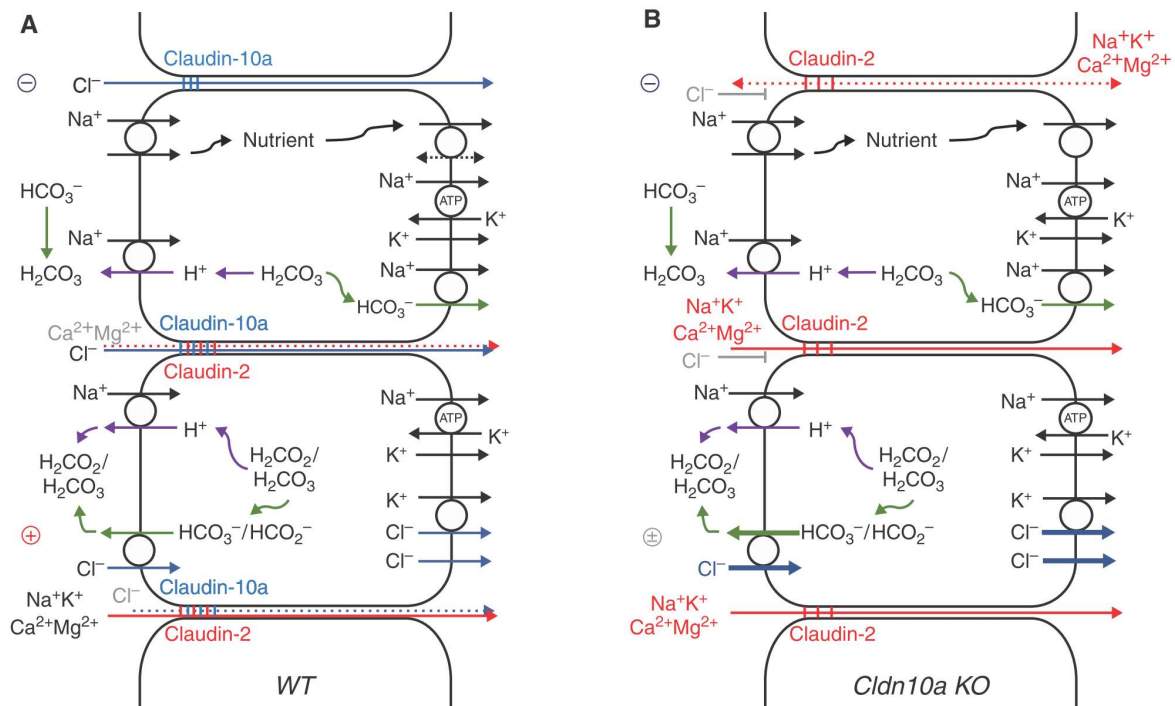
Fig. 8: Schematic model of transepithelial transport in proximal tubule (PT, lumen left).

A In the WT, the early PT is represented in the upper part where the major transport activity is reabsorption of filtered HCO_3^- and nutrients like glucose. Both are fueled by the Na^+ gradient into the cell and energized by the basolateral Na^+/K^+-ATPase. Since luminal substrate transport is electrogenic and leaves a negative charge in the lumen, this negative voltage can push paracellular Cl^- reabsorption via claudin-10a. As water is reabsorbed in parallel and as Cl^- and HCO_3^- together sum up to balance cation charges, Cl^- concentration still rises along the PT. Now, Cl^- can passively diffuse along its gradient via claudin-10a towards the basolateral side, leaving a positive charge behind. The respective lumen positive voltage facilitates paracellular reabsorption of Ca^{2+} and Mg^{2+} which occurs along the concentration gradient towards the basolateral side due to water reabsorption. The late proximal tubule (lower part) is further equipped to transport Cl^- via the transcellular route. Cl^- is taken up into the cell via anion exchange and may leave the cell together with K^+ either by cotransport or ion channels. The exchanged anions (e. g., formate or bicarbonate) form membrane permeant uncharged acids after protonation from Na^+/H^+ exchange into the lumen. Then, they recycle across the luminal membrane to keep the system running. Basolateral equipment by K^+ channels and electrogenic Na^+/K^+-ATPase provide the negative cell membrane voltage to run Na^+ coupled HCO_3^- exit and Cl^- extrusion, respectively. Many other transport systems have been omitted for simplicity of the scheme.

B In claudin-10a deficiency, this model suggests several PT functions to be affected: i) breakdown of paracellular Cl^- reabsorption in early PT. ii) breakdown of late PT lumen positive voltage. iii) transcellular backleak of HCO_3^- into the lumen (increased Cl^-/HCO_3^- exchange,

raising luminal pH). iv) increased paracellular diffusion of Ca^{2+} and Mg^{2+} (along their concentration gradients) as claudin-2 spreads into tight junctions all along the PT. In consequence, the proximal tubule via transcellular transport and the downstream nephron segments have to compensate accordingly.

Supplemental Materials

Table of Contents

Supplemental Table 1: Oligonucleotides.

The following oligonucleotides were used to amplify the 5`homology region (HR5), the floxed region (FR), the 3`homology region (HR3), and the Southern Blot probe. The primers used for genotyping are labeled with "geno".

oligonucleotide	sequence 5' - 3'
HR5_for	GACATTTGTGAGGCTAAAACTCC
HR5_rev	ATCTTCCTAGATGATTCTGGATTACC
FR_for	GTGTTTCCAGCACACTGGCA
FR_rev	ACACCCATAAAAATTTCTCTGTGAC
HR3_rev	CTTCTCAATGACTTCCCTTGC
HR3_for	TGAAAGGTCTTTCATTGATTTAGAATC
probe_for	AGGTGGATCTTTCTTGCCC
probe_rev	AGAAGCCGAAGCTAGCTCTC
geno_WT_for	TCCAATGCAAAGTGTAGGAAGTG
geno_KO_for	TTCTGTTAGTGCCACAACGC
geno_rev	TCATGGCGCTTCCTTTCAACTG

Supplemental Table 2: Antibodies used for Western blotting and immunofluorescence staining.

Ab #	Antibody	Dilution	Vendor	Antibody Registry ID	Application
1	Mouse anti-claudin-2	1:1000	Thermo Fischer Scientific	AB_2533085	Western Blot
2	Rabbit anti-claudin-10	1:1000	Thermo Fischer Scientific	AB_2533386	Western Blot
3	Rabbit anti-aquaporin 2	1:1000	Novus Biologicals	AB_1107363	Western Blot
4	Rabbit anti-NKCC2	1:1000	StressMarq Biosciences	AB_10640877	Western Blot
5	pNCC S71	1:1000	Pineda Anti-bodies Service	NA[5]	Western Blot
6	Rabbit anti-NCC	1:1000	StressMarq Biosciences	AB_10641430	Western Blot
7	Mouse anti-β-actin	1:5000	Sigma-Aldrich	AB_476692	Western Blot
8	Mouse anti-tubulin	1:4000	Sigma-Aldrich	AB_477593	Western Blot
9	Rabbit anti-claudin-2	1:400	Thermo Fischer Scientific	AB_2533911	Immunofluorescence Staining
10	Mouse anti-claudin-10	1:400	Thermo Fischer Scientific	AB_2533510	Immunofluorescence Staining
11	Goat anti-rabbit IgG Alexa 633	1:400	Thermo Fischer Scientific	AB_2535731	Immunofluorescence Staining
12	Goat anti-mouse IgG Alexa 488	1:400	Thermo Fischer Scientific	AB_2534084	Immunofluorescence Staining
13	Mouse anti-claudin-1	1:200	Thermo Fischer Scientific	AB_2533323	Immunofluorescence Staining
14	Mouse anti-claudin-2	1:200	Thermo Fischer Scientific	AB_2533085	Immunofluorescence Staining
15	Rabbit anti-claudin-10	1:200	Thermo Fischer Scientific	AB_2533386	Immunofluorescence Staining
16	Rabbit anti-claudin-12	1:100	NA[1]	NA[1]	Immunofluorescence Staining
17	Rabbit anti-Na-PiIIa	1:500	NA[2]	NA[3]	Immunofluorescence Staining
18	Mouse anti-NHE3	1:500	Millipore	AB_94714	Immunofluorescence Staining
19	Guinea pig anti-NKCC2	1:2000	Pineda Anti-bodies Service	NA[2]	Immunofluorescence Staining
20	Rabbit anti-NCC	1:500	NA[4]	NA[5]	Immunofluorescence Staining
21	Rabbit anti-phospho-S71-NCC	1:20000	Pineda Anti-bodies Service	NA[5]	Immunofluorescence Staining
22	Goat anti-aquaporin 2	1:500	Santa Cruz Biotechnology	AB_10988758	Immunofluorescence Staining
23	Goat anti-rabbit IgGF Cγ2	1:200	Jackson/Dianova	AB_2338747	Immunofluorescence Staining

24	Goat anti-mouse IgGF Cγ3	1:300	Jackson/Dianova	AB_2338694	Immunofluorescence Staining
25	Donkey anti-guinea pig IgGF Cγ3	1:300	Jackson/Dianova	AB_2340467	Immunofluorescence Staining
26	Donkey anti-goat IgGF Cγ3	1:300	Jackson/Dianova	AB_2307341	Immunofluorescence Staining
27	Rabbit anti-occludin	1:100	Thermo Fischer Scientific	AB_2533977	Immunofluorescence Staining
28	Rabbit anti-ZO-1	1:200	Thermo Fischer Scientific	AB_2533456	Immunofluorescence Staining
29	Goat anti-Rabbit IgG Alexa 488	1:400	Thermo Fischer Scientific	AB_2576217	Immunofluorescence Staining
30	Goat anti-mouse IgG Alexa 594	1:400	Thermo Fischer Scientific	AB_2534091	Immunofluorescence Staining

[1]kind gift of Dr. H. Rittner, Würzburg, Germany
[2]Mutig et al., 2007, Am J Physiol Renal Physiol. 293:F1166-F1177
[3]kind gift of Dr. J. Biber, Zurich, Switzerland; see also Bachmann et al., 2004, J Am Soc Nephrol. 15:892-900
[4]kind gift of Dr. D. H. Ellison, Portland, Oregon, USA
[5]see also Mutig et al., 2010, Am J Physiol Renal Physiol. 298:F502-F509

Supplemental Table 3: Transepithelial voltage and resistance of isolated PT segments in NaCl-based control solution.

Transepithelial Voltage (V_{te}, mV)		S1	PCT	S2	S3
WT	MW ± SEM	-0.02 ± 0.09	-0.32 ± 0.13	-0.24 ± 0.17	-1.18 ± 0.36
	n	11	14	7	10
Cldn10a KO	MW ± SEM	0.25 ± 0.16	0.14 ± 0.21	-0.30 ± 0.23	-1.47 ± 0.37
	n	10	11	9	7
	p-value	ns	ns	ns	**0.04**
Transepithelial Resistance (R_{te}, $\Omega \cdot cm^2$)					
WT	MW ± SEM	6.4 ± 1.5	10.6 ± 2.2	9.3 ± 1.6	9.3 ± 1.20
	n	11	14	8	8
Cldn10a KO	MW ± SEM	8.0 ± 1.8	5.9 ± 1.8	5.7 ± 2.0	11.3 ± 2.3
	n	10	11	9	7
	p-value	ns	ns	ns	ns

Supplemental Table 4: Transepithelial voltage and resistance of isolated PT segments in Na-pyruvate-based solution.

Transepithelial Voltage (V_{te}, mV)		S1	PCT	S2	S3
WT	MW ± SEM	0.30 ± 0.15	-0.03 ± 0.16	-0.87 ± 0.13	-2.74 ± 0.35
	n	16	20	19	16
Cldn10a KO	MW ± SEM	0.28 ± 0.13	0.13 ± 0.17	-0.68 ± 0.26	-2.63 ± 0.29
	n	15	11	9	7
	p-value	ns	ns	ns	ns
Transepithelial Resistance (R_{te}, $\Omega \cdot cm^2$)					
WT	MW ± SEM	5.5 ± 0.6	6.4 ± 1.0	5.6 ± 0.6	7.8 ± 0.7
	n	16	20	19	16
Cldn10a KO	MW ± SEM	3.6 ± 0.6	5.9 ± 0.8	5.0 ± 0.7	6.4 ± 0.7
	n	15	11	9	7
	p-value	**0.03**	ns	ns	ns

Supplemental Table 5: Transepithelial voltage, transepithelial resistance, and furosemide inhibitable transport current in cortical thick ascending limb segments.

		Transepithelial Voltage (V_{te}, mV)	Transepithelial Resistance (R_{te}, $\Omega \cdot cm^2$)	$\Delta I'sc_{furo}$ [$\mu A/cm^2$]
WT	MW ± SEM	18.0 ± 1.2	11.3 ± 1.0	-1486 ± 129
	n	13	13	13
Cldn10a KO	MW ± SEM	16.8 ± 0.9	10.0 ± 0.8	-1728 ± 183
	n	17	17	17
	p-value	ns	ns	ns

Supplemental Table 6A: Reads per kilobase of transcript, per million mapped reads for Claudins 1 to 24 in isolated WT and *Cldn10a* KO PCT and DCT.

	PCT				DCT	
	WT	***Cldn10a* KO**			**WT**	***Cldn10a* KO**
CLDN1	**2.95 ± 0.65**	**2.35 ± 0.55**	CLDN1		0.01 ± 0.00	0.04 ± 0.02
CLDN2	**54.03 ± 5.73**	**56.19 ± 4.16**	CLDN2		0.09 ± 0.04	0.08 ± 0.04
CLDN3	n.d.	n.d.	CLDN3		0.45 ± 0.04	0.34 ± 0.11
CLDN4	n.d.	n.d.	**CLDN4**		**1.45 ± 0.22**	**1.50 ± 0.32**
CLDN5	n.d.	n.d.	CLDN5		n.d.	0.02 ± 0.02
CLDN6	0.34 ± 0.12	0.32 ± 0.19	CLDN6		0.33 ± 0.08	0.66 ± 0.19
CLDN7	n.d.	0.01 ± 0.01	**CLDN7**		**2.19 ± 0.34**	**1.68 ± 0.19**
CLDN8	0.02 ± 0.01	n.d.	**CLDN8**		**29.95 ± 0.84**	**28.91 ± 1.52**
CLDN9	n.d.	n.d.	CLDN9		0.10 ± 0.05	0.17 ± 0.13
CLDN10	**10.11 ± 2.63**	**n.d.**	CLDN10		0.08 ± 0.04	0.07 ± 0.04
CLDN11	n.d.	n.d.	CLDN11		n.d.	n.d.
CLDN12	**7.49 ± 0.50**	**7.94 ± 0.45**	**CLDN12**		**1.72 ± 0.15**	**1.37 ± 0.02**
CLDN13	n.d.	n.d.	CLDN13		n.d.	n.d.
CLDN14	n.d.	n.d.	CLDN14		n.d.	n.d.
CLDN15	0.20 ± 0.06	0.14 ± 0.07	CLDN15		0.32 ± 0.04	0.22 ± 0.04
CLDN16	n.d.	n.d.	**CLDN16**		**1.23 ± 0.38**	**1.60 ± 0.31**
CLDN17	n.d.	n.d.	CLDN17		0.02 ± 0.02	n.d.
CLDN18	0.07 ± 0.01	0.19 ± 0.05	CLDN18		n.d.	n.d.
CLDN19	n.d.	n.d.	CLDN19		0.33 ± 0.13	0.28 ± 0.04
CLDN20	0.07 ± 0.05	0.03 ± 0.03	CLDN20		0.05 ± 0.03	0.04 ± 0.02
CLDN22	n.d.	n.d.	CLDN22		n.d.	n.d.
CLDN23	n.d.	n.d.	CLDN23		n.d.	0.02 ± 0.02
CLDN24	0.02 ± 0.02	n.d.	CLDN24		0.02 ± 0.02	n.d.

means ± SEM; PCT, n = 4 WT and 3 KO mice; DCT, n = 4 WT and 4 KO mice. Values > 1 are highlighted in **bold**.

Supplemental Table 6B: Whole kidney RNA array analysis.

Gene Symbol	Fold-Change *Cldn10a* KO vs. WT	p-value *Cldn10a* KO vs. WT
Cldn1	1.10	0.771
Cldn2	1.31	0.193
Cldn3	1.18	0.560
Cldn4	1.16	0.607
Cldn5	-1.11	0.144
Cldn6	-1.01	0.919
Cldn7	-1.54	0.005
Cldn8	1.45	0.288
Cldn9	-1.18	0.531
Cldn10(a+b)	**-4.39**	**0.089**
Cldn11	-1.07	0.615
Cldn12	1.19	0.379
Cldn13	-1.24	0.272
Cldn14	1.15	0.464
Cldn15	-1.37	0.195
Cldn16	-1.13	0.661
Cldn17	-1.08	0.724
Cldn18	1.25	0.154
Cldn19	1.20	0.345
Cldn20	-1.02	0.947
Cldn22	-1.40	0.032
Cldn23	-1.04	0.858
Cldn24	1.15	0.652
Slc12a1	-1.07	0.403
Slc12a3	-1.01	0.963
Aqp2	-1.35	0.402

RNA was extracted from 3 WT and 3 *Cldn10a* KO whole mouse kidneys using the NucleoSpin RNA/Protein, Mini kit for RNA and protein purification (Macherey-Nagel, Düren, Germany), according to the manufacturer's instructions. Clariom S Affymetrix mouse array analysis was conducted at the Charité core facility (Charité – Universitätsmedizin Berlin, Germany). No conclusive pattern emerged from these data, as effects on specific nephron segments are diluted in such a whole kidney approach. However, the data suggest that there are no relevant overall changes in any of the claudins, especially not in claudin-16 and -19, which would be decisive to the reabsorption of divalent cations.
Note that this approach is not able to discriminate between *Cldn10a* and *Cldn10b* as it measures total *Cldn10*.
Major transporters found to be upregulated in Western Blots and immunostainings (NKCC2 = Slc12a1, NCC = Slc12a3, Aqp2) were also unaltered in this analysis.

Supplemental Table 7A: Comparison of urine parameters between WT and *Cldn10a* KO mice after treatment with acetazolamide, furosemide, and hydrochlorothiazide, respectively.

Urine		Volume (ml/h)	Osmola-rity (mOsM)	Urea (mM)	pH	Crea-tinine (mM)	Na (mM)	K (mM)	Ca (mM)	Mg (mM)	Cl (mM)	Phos-phate (mM)
Acetazolamide												
WT	**MW ± SEM**	0.05 ± 0.01	1118.6 ± 44.6	480.1 ± 89.0	7.78 ± 0.08	1.30 ± 0.12	171.8 ± 5.4	208.0 ± 6.9			118.5 ± 8.4	30.4 ± 2.8
	n	8	8	8	8	8	8	8			8	8
Cldn10a KO	**MW ± SEM**	0.04 ± 0.01	1174.1 ± 99.6	531.6 ± 83.5	8.10 ± 0.10	1.13 ± 0.14	175.8 ± 12.1	246.9 ± 13.5			141.3 ± 19.8	26.8 ± 4.7
	n	8	8	8	8	8	8	8			8	8
	p-value	ns	ns	ns	**0.04**	ns	ns	**0.03**			ns	ns
Furosemide												
WT	**MW ± SEM**	0.25 ± 0.03	480.3 ± 24.6	96.1 ± 15.9	6.88 ± 0.27	0.60 ± 0.10	132.3 ± 6.8	47.81 ± 3.97	0.77 ± 0.04		154.5 ± 7.1	
	n	8	8	8	8	8	8	8	8		8	
Cldn10a KO	**MW ± SEM**	0.24 ± 0.04	475.4 ± 57.8	55.6 ± 8.3	8.00 ± 0.30	0.42 ± 0.09	163.5 ± 16.3	38.14 ± 5.05	0.83 ± 0.04		189.4 ± 19.6	
	n	8	8	8	8	8	8	7	8		8	
	p-value	ns	ns	**0.04**	**0.014**	ns	ns	ns	ns		ns	
Hydrochlorothiazide												
WT	**MW ± SEM**	0.13 ± 0.01	688.4 ± 65.3	262.3 ± 48.1		0.95 ± 0.14	172.8 ± 9.4	106.5 ± 13.8		0.57 ± 0.07	172.8 ± 17.5	
	n	8	8	8		8	8	7		4	8	
Cldn10a KO	**MW ± SEM**	0.16 ± 0.03	607.6 ± 41.8	215.1 ± 31.6		0.65 ± 0.09	171.1 ± 4.2	90.8 ± 9.8		0.46 ± 0.08	175.6 ± 6.5	
	n	8	8	8		8	8	8		3	8	
	p-value	ns	ns	ns		ns	ns	ns		ns	ns	

Supplemental Table 7B: Comparison of serum parameters between WT and *Cldn10a* KO mice after treatment with furosemide and hydrochlorothiazide, respectively.

Serum		Osmolarity (mOsM)	Creatinine (µM)	Na (mM)	K (mM)	Ca (mM)	Mg (mM)	Cl (mM)
Furosemide								
WT	**MW ± SEM**	307.3 ± 0.9	9.82 ± 1.15	142.6 ± 0.7	4.81 ± 0.27	0.58 ± 0.05		99.4 ± 1.9
	n	7	8	7	8	7		7
***Cldn10a* KO**	**MW ± SEM**	317.5 ± 5.2	12.36 ± 1.63	146.8 ± 2.0	4.31 ± 0.22	0.71 ± 0.07		99.8 ± 1.6
	n	6	7	6	7	6		6
	p-value	ns	ns	ns	ns	ns		ns
Hydrochlorothiazide								
WT	**MW ± SEM**	312.7 ± 2.7	12.5 ± 2.0	143.6 ± 1.0	4.22 ± 0.24	0.83 ± 0.10	0.53 ± 0.06	110.7 ± 2.2
	n	3	7	7	7	7	4	7
***Cldn10a* KO**	**MW ± SEM**	308.0 ± 6.2	12.2 ± 1.2	146.7 ± 2.4	3.96 ± 0.24	0.76 ± 0.09	0.53 ± 0.09	106.8 ± 1.9
	n	2	6	6	6	6	4	6
	p-value	ns	ns	ns	ns	ns	ns	ns

Due to small serum volumes obtained, values are missing for the acetazolamide experiment.

Supplemental Table 7C: Comparison of fractional excretion between WT and *Cldn10a* KO mice. Values after treatment with furosemide and hydrochlorothiazide, respectively.

		Fractional Excretion (%)				
		Na	K	Ca	Cl	Mg
Furosemide						
WT	**MW ± SEM**	1.63 ± 0.48	18.91 ± 3.48	2.37 ± 0.65	2.74 ± 0.83	
	n	7	8	7	7	
***Cldn10a* KO**	**MW ± SEM**	5.31 ± 2.00	34.19 ± 4.57	6.13 ± 2.46	9.02 ± 3.38	
	n	7	7	7	7	
	p-value	ns	**0.02**	ns	ns	
Hydrochlorothiazide						
WT	**MW ± SEM**	1.71 ± 0.45	34.74 ± 9.86		2.11 ± 0.52	1.66 ± 0.89
	n	8	7		8	4
***Cldn10a* KO**	**MW ± SEM**	2.82 ± 0.51	43.66 ± 6.76		3.87 ± 0.60	1.59 ± 0.31
	n	8	8		8	3
	p-value	ns	ns		**0.04**	ns

Supplemental Table 7D: Comparison of renal clearance between WT and *Cldn10a* KO mice. Values after treatment with furosemide and hydrochlorothiazide, respectively.

		Clearance (ml/min)					
		Na	K	Ca	Cl	Mg	Creatinine
Furosemide							
WT	**MW ± SEM**	0.0039 ± 0.0003	0.0423 ± 0.0044	0.0059 ± 0.0008	0.0065 ± 0.0005		0.2923 ± 0.0575
	n	7	8	7	7		8
***Cldn10a* KO**	**MW ± SEM**	0.0041 ± 0.0007	0.0423 ± 0.0093	0.0049 ± 0.0011	0.0071 ± 0.0011		0.1227 ± 0.0334
	n	7	6	7	7		8
	p-value	ns	ns	ns	ns		**0.02**
Hydrochlorothiazide							
WT	**MW ± SEM**	0.0026 ± 0.0002	0.0513 ± 0.0090		0.0033 ± 0.0003	0.0023 ± 0.0004	0.2204 ± 0.0516
	n	8	7		8	4	8
***Cldn10a* KO**	**MW ± SEM**	0.0030 0.0006	0.0512 0.0106		0.0042 0.0007	0.0023 0.0009	0.1247 0.0298
	n	8	8		8	3	8
	p-value	ns	ns		ns	ns	ns

Supplemental Table 8: Enrichment (p-value cutoff 0.01) of GO terms in differentially expressed genes of the PCT samples. The source column refers to the Gene Ontology subdomains: molecular function (MF), cellular component (CC), biological process (BP).

P-value	Term size	Intersection size	Term id	Source	Term name
1.43E-17	1726	52	GO:0044281	GO:BP	small molecule metabolic process
7.95E-16	948	38	GO:0006082	GO:BP	organic acid metabolic process
4.57E-13	898	34	GO:0019752	GO:BP	carboxylic acid metabolic process
7.01E-13	911	34	GO:0043436	GO:BP	oxoacid metabolic process
3.54E-11	425	23	GO:0006631	GO:BP	fatty acid metabolic process
2.04E-10	616	26	GO:0032787	GO:BP	monocarboxylic acid metabolic process
1.06E-09	5913	83	GO:0003824	GO:MF	catalytic activity
2.18E-09	1349	36	GO:0006629	GO:BP	lipid metabolic process
4.29E-09	296	18	GO:0006790	GO:BP	sulfur compound metabolic process
1.10E-08	992	30	GO:0044255	GO:BP	cellular lipid metabolic process
2.54E-06	334	16	GO:0016042	GO:BP	lipid catabolic process
3.62E-06	150	11	GO:0042579	GO:CC	microbody
3.62E-06	150	11	GO:0005777	GO:CC	peroxisome
3.56E-05	368	15	GO:0033218	GO:MF	amide binding
3.97E-05	141	10	GO:0016616	GO:MF	oxidoreductase activity
8.06E-05	152	10	GO:0016614	GO:MF	oxidoreductase activity
9.66E-05	618	19	GO:0044283	GO:BP	small molecule biosynthetic process
0.00011939	109	9	GO:0033865	GO:BP	nucleoside bisphosphate metabolic process
0.00011939	109	9	GO:0033875	GO:BP	ribonucleoside bisphosphate metabolic process
0.00011939	109	9	GO:0034032	GO:BP	purine nucleoside bisphosphate metabolic process
0.00013749	7	4	GO:0019694	GO:BP	alkanesulfonate metabolic process
0.00013749	7	4	GO:0019530	GO:BP	taurine metabolic process
0.00023406	293	13	GO:0016053	GO:BP	organic acid biosynthetic process
0.00026747	831	21	GO:0016491	GO:MF	oxidoreductase activity
0.00029722	59	7	GO:0006749	GO:BP	glutathione metabolic process
0.00038056	818	21	GO:0055114	GO:BP	oxidation-reduction process
0.00051096	169	10	GO:0006575	GO:BP	cellular modified amino acid metabolic process
0.00063433	218	11	GO:0046395	GO:BP	carboxylic acid catabolic process
0.00071955	98	8	GO:0009062	GO:BP	fatty acid catabolic process
0.00090813	226	11	GO:0016054	GO:BP	organic acid catabolic process
0.00096343	181	10	GO:1901605	GO:BP	alpha-amino acid metabolic process
0.00126978	285	12	GO:0046394	GO:BP	carboxylic acid biosynthetic process
0.00143572	258	11	GO:1901681	GO:MF	sulfur compound binding
0.00143855	74	7	GO:0006635	GO:BP	fatty acid beta-oxidation

0.00145554	344	13	GO:0044282	GO:BP	small molecule catabolic process
0.00214532	113	8	GO:0019395	GO:BP	fatty acid oxidation
0.00242128	1978	33	GO:1901575	GO:BP	organic substance catabolic process
0.00261761	116	8	GO:0009410	GO:BP	response to xenobiotic stimulus
0.00309255	5944	68	GO:0043167	GO:MF	ion binding
0.00312254	36	5	GO:0004364	GO:MF	glutathione transferase activity
0.00317573	119	8	GO:0034440	GO:BP	lipid oxidation
0.00360156	121	8	GO:0072329	GO:BP	monocarboxylic acid catabolic process
0.00404628	18	4	GO:0043295	GO:MF	glutathione binding
0.00423085	213	10	GO:0044242	GO:BP	cellular lipid catabolic process
0.00456601	73	6	GO:0031526	GO:CC	brush border membrane
0.00509698	19	4	GO:1900750	GO:MF	oligopeptide binding
0.00513691	15	4	GO:0015936	GO:BP	coenzyme A metabolic process
0.00517996	68	6	GO:0016765	GO:MF	transferase activity
0.00602702	521	15	GO:0010876	GO:BP	lipid localization
0.00634034	11132	105	GO:0005737	GO:CC	cytoplasm
0.00673917	459	14	GO:0006869	GO:BP	lipid transport
0.00773682	134	8	GO:0006690	GO:BP	icosanoid metabolic process
0.00848765	36	5	GO:0009069	GO:BP	serine family amino acid metabolic process

Supplemental Table 9: Separate Excel file of transcriptome data:

pct_wt_vs_ko_diff_expr_genes.xlsx
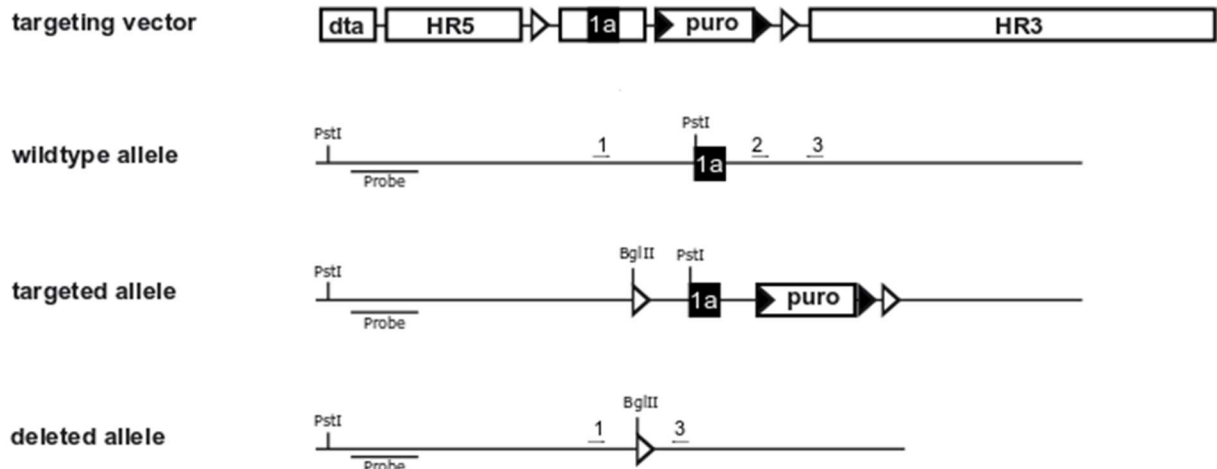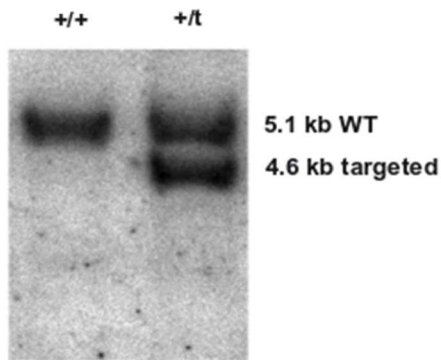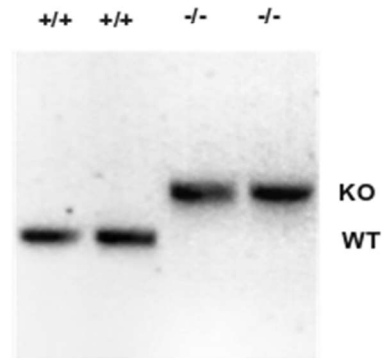
Supplemental Figure 1: Generation of a *Cldn10a* KO mouse.

A Strategy for the targeting of exon 1a of *Cldn10a.* For the generation of a floxed exon 1a of *Cldn10*a targeting construct was generated in which a loxP site was inserted before the floxed region (FR, 1.3 kb) containing exon 1a. The 5´homology region (HR5, 2.0 kb) was flanked by a dta (Diphteria Toxin A) cassette. A puromycin resistance cassette together with the second loxP site was inserted between the FR and the 3´homology region (HR3, 12 kb).

B Southern Blot of the targeted embryonic stem cells clone. The targeted clone showed an additional band of the correct size.

C Genotyping of tissue samples from mice. PCR using the three primers 1,2, and 3 confirmed the absence of the WT allele in *Cldn10a* KO mice.
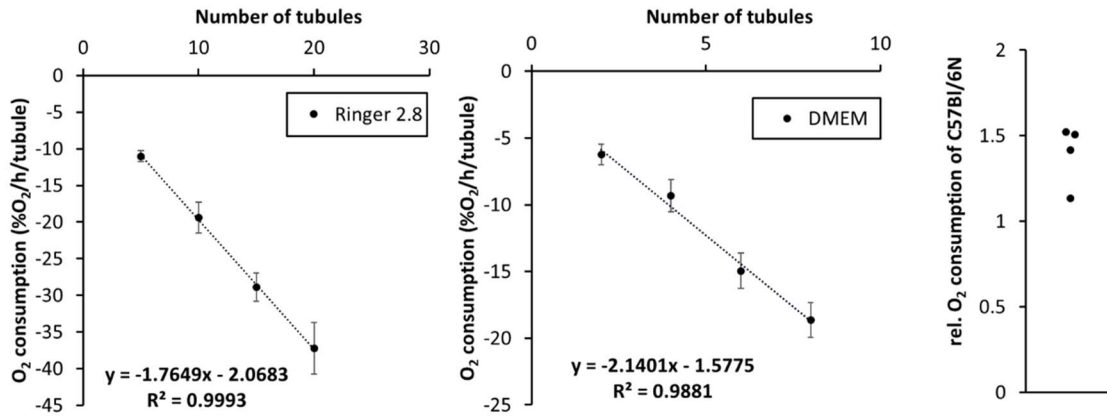
Supplemental Figure 2: O_2 experiment: calibration curve.

O_2 consumption was calibrated to the number of proximal convoluted tubules (PCT).

Left panel: minimal solution calibration curve with 5, 10, 15, and 20 PCT.

Middle panel: DMEM calibration curve with 2, 4, 6, and 8 PCT.

Right panel: calculated relative O_2 consumption as ratio between mean O_2 consumption for all measurements in minimal solution and DMEM, respectively. N = 4 mice.
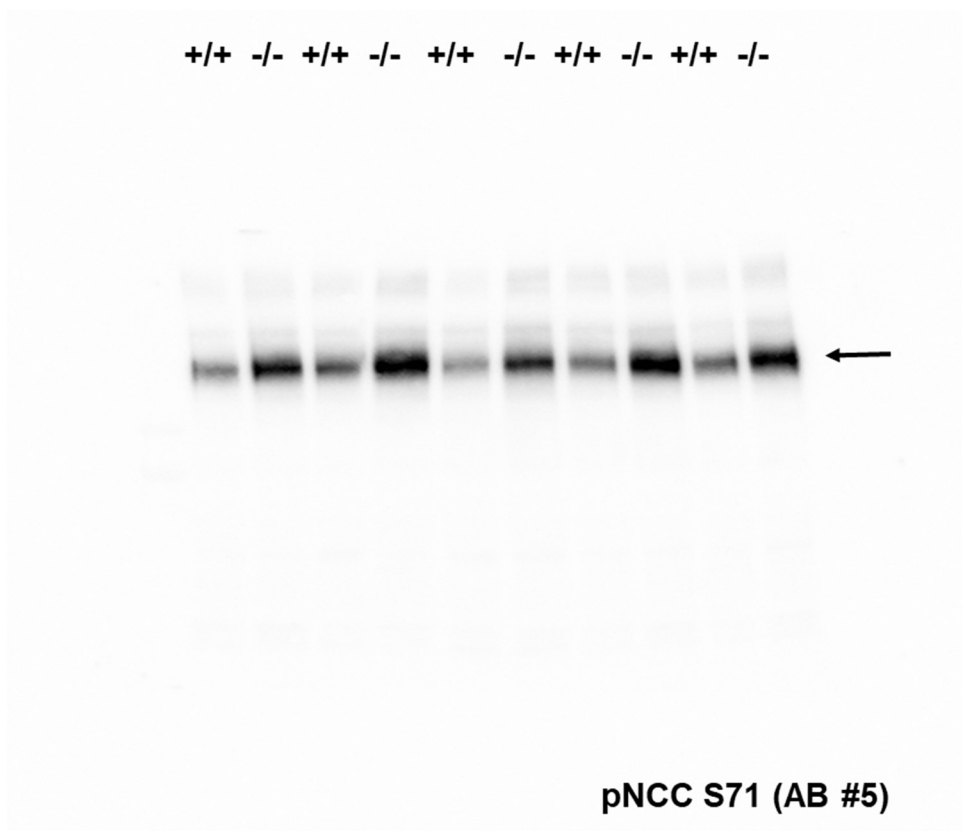
Supplemental Figure 3: Western blots: linearity.
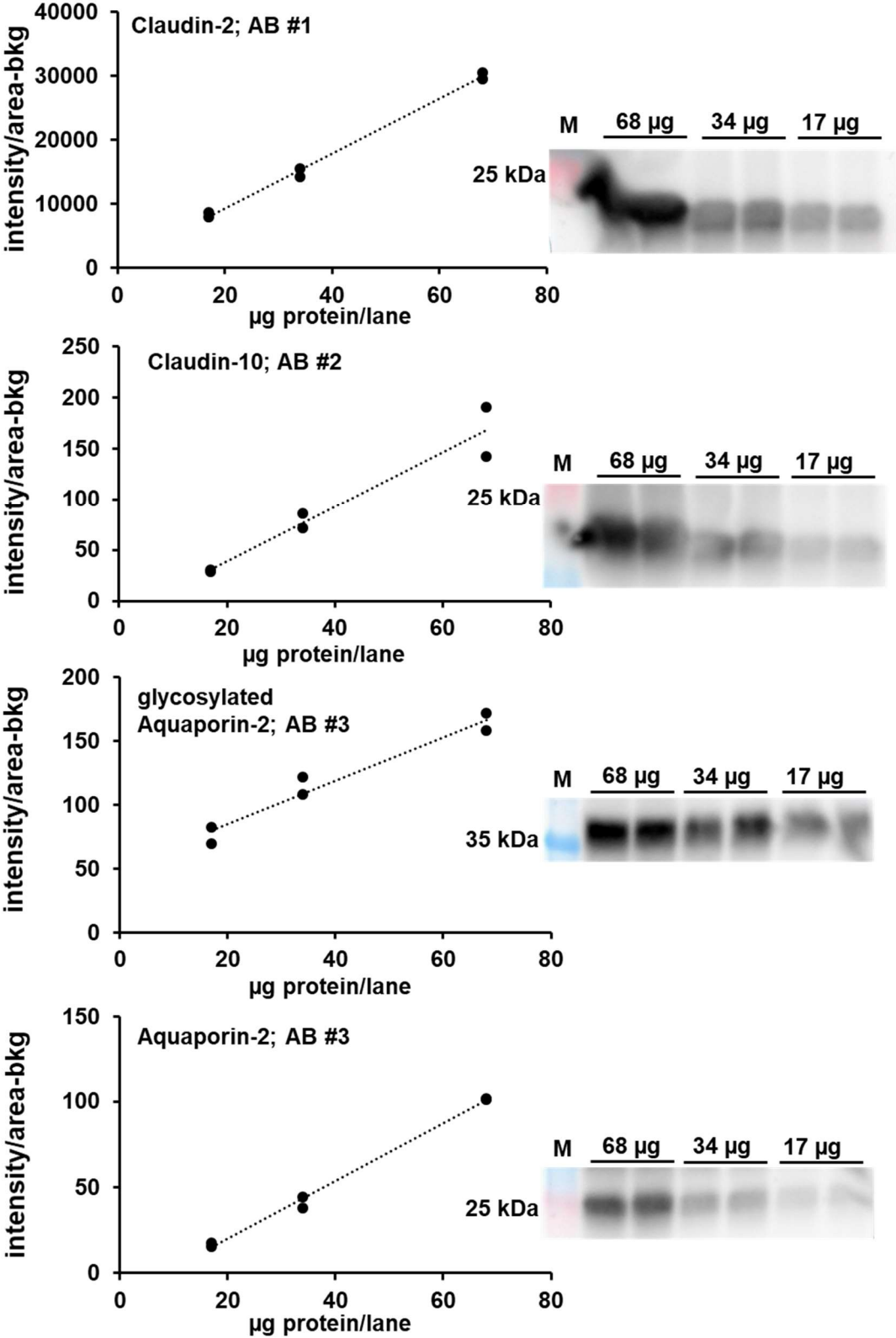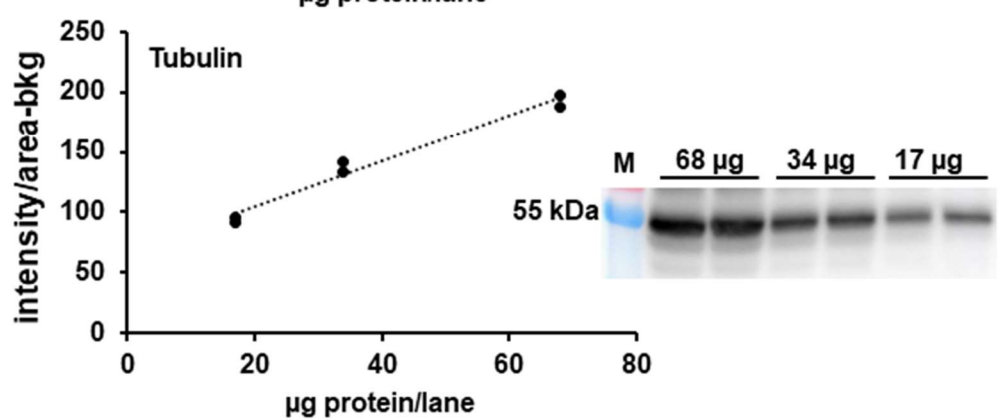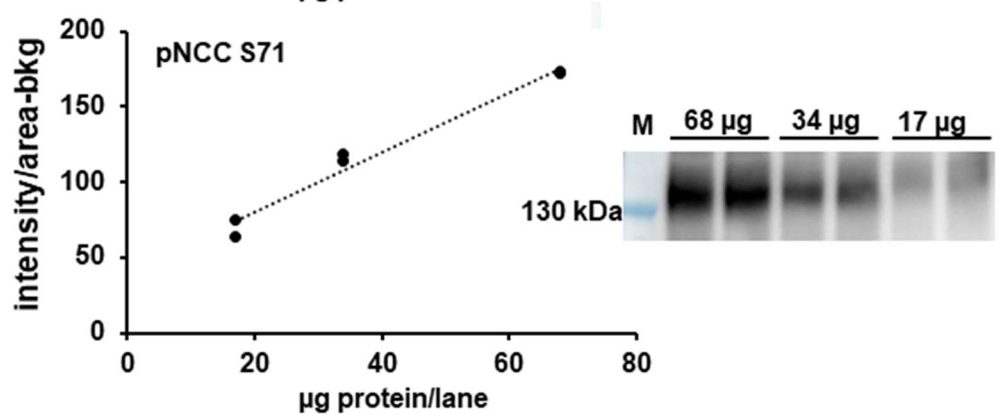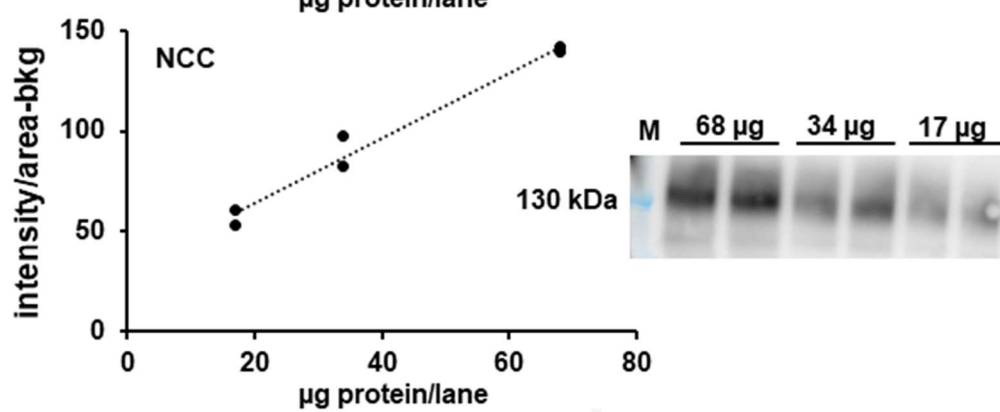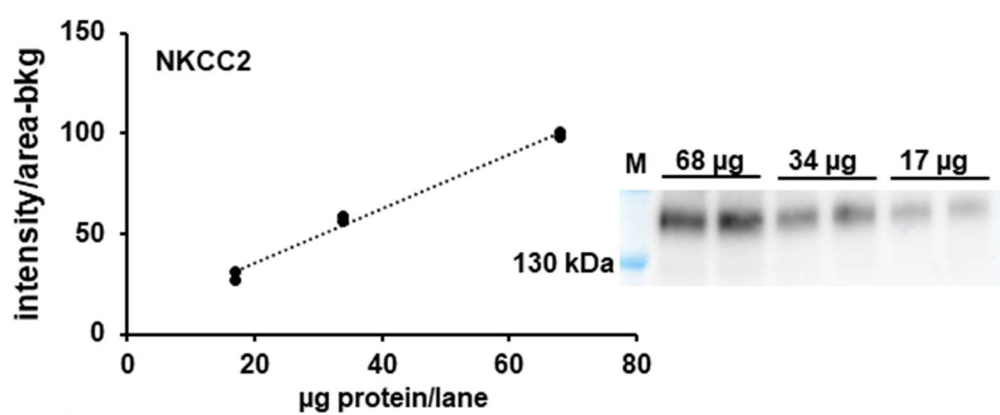
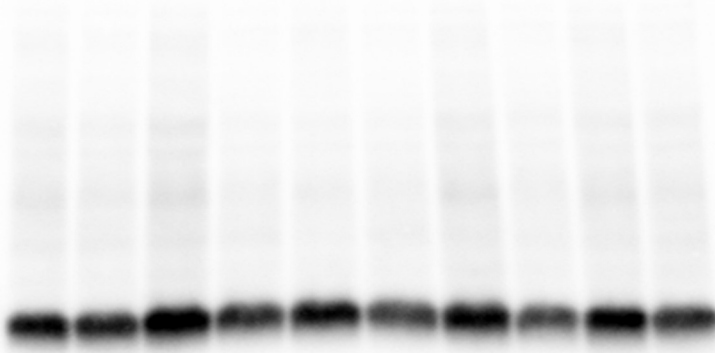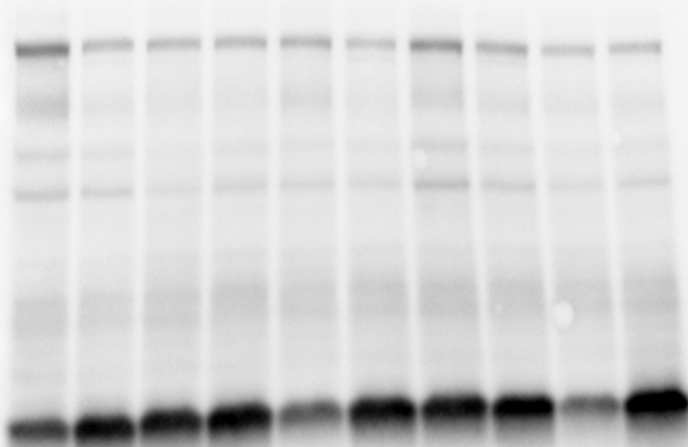**Supplemental Figure 4: Original Western blots.**

Original blots, Fig. 1

+/+ -/- +/+ -/- +/+ -/- +/+ -/- +/+ -/-

Claudin-2 (AB #1)

+/+ -/- +/+ -/- +/+ -/- +/+ -/- +/+ -/-

Tubulin (AB #8)

Original blots, Fig. 4

NKCC2 (AB #4)

pNCC S71 (AB #5)

NCC (AB #6)

glycosylated
Aquaporin-2

Aquaporin-2

AQP-2 (AB #3)

Tubulin (AB #8)
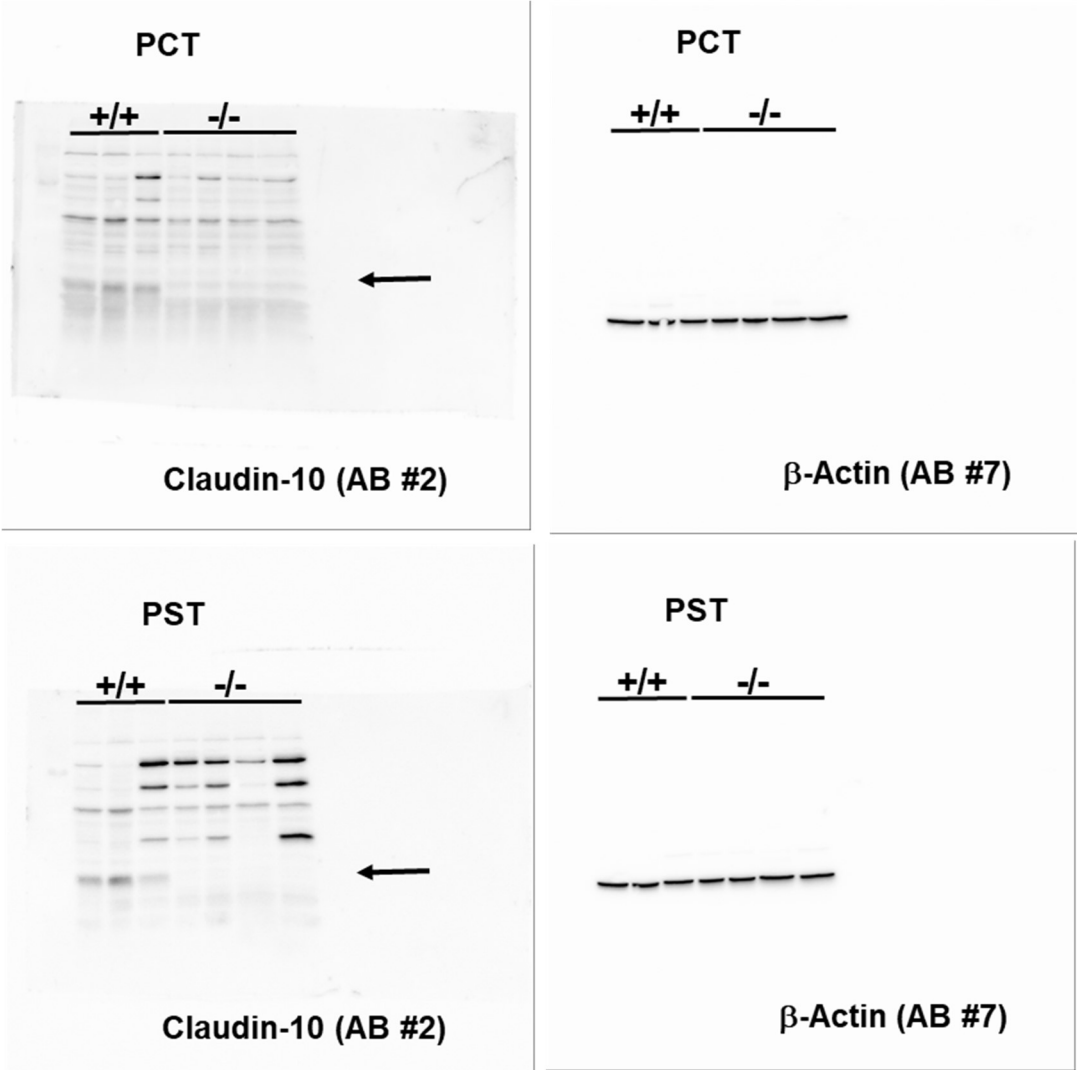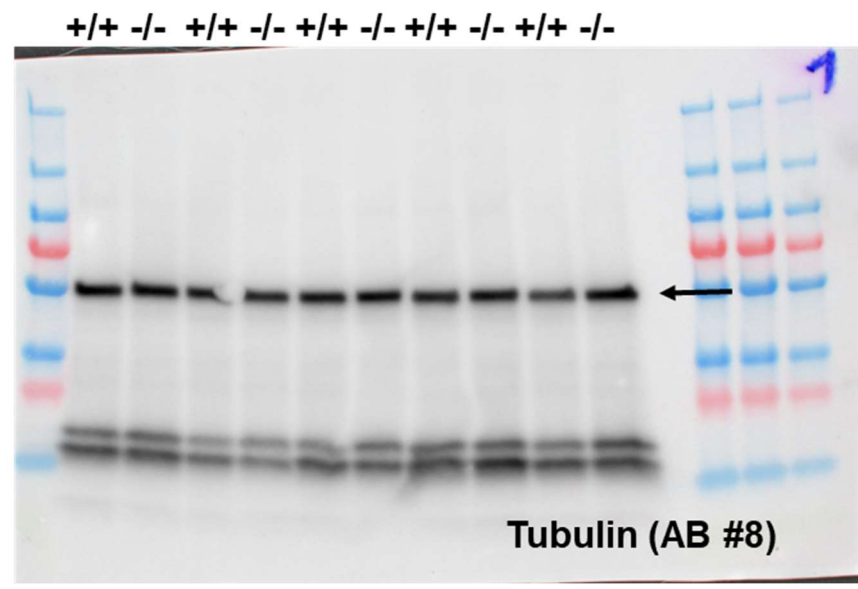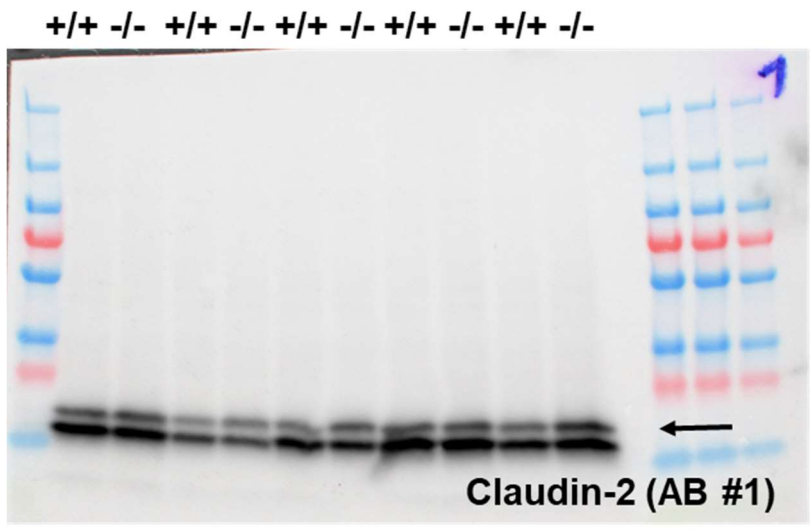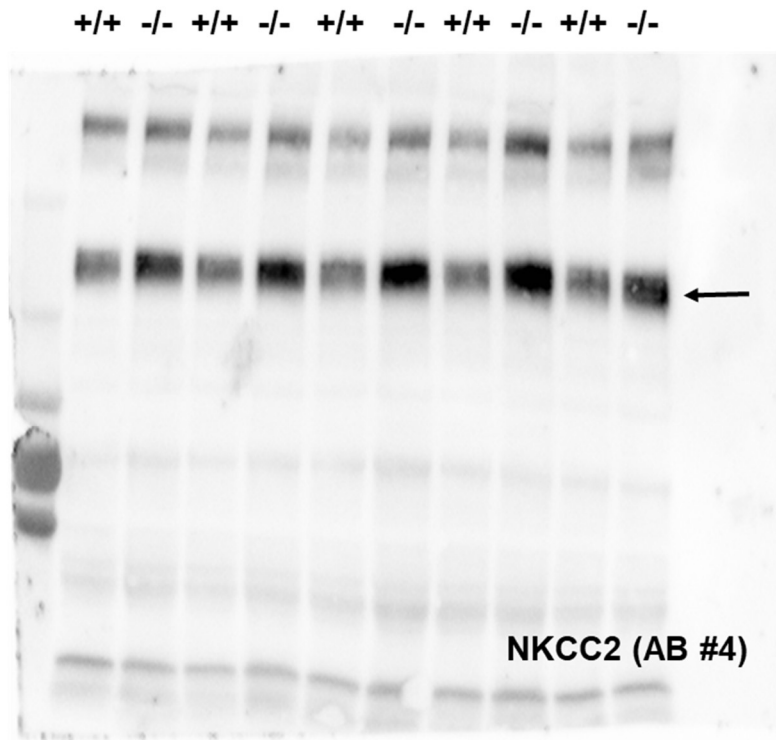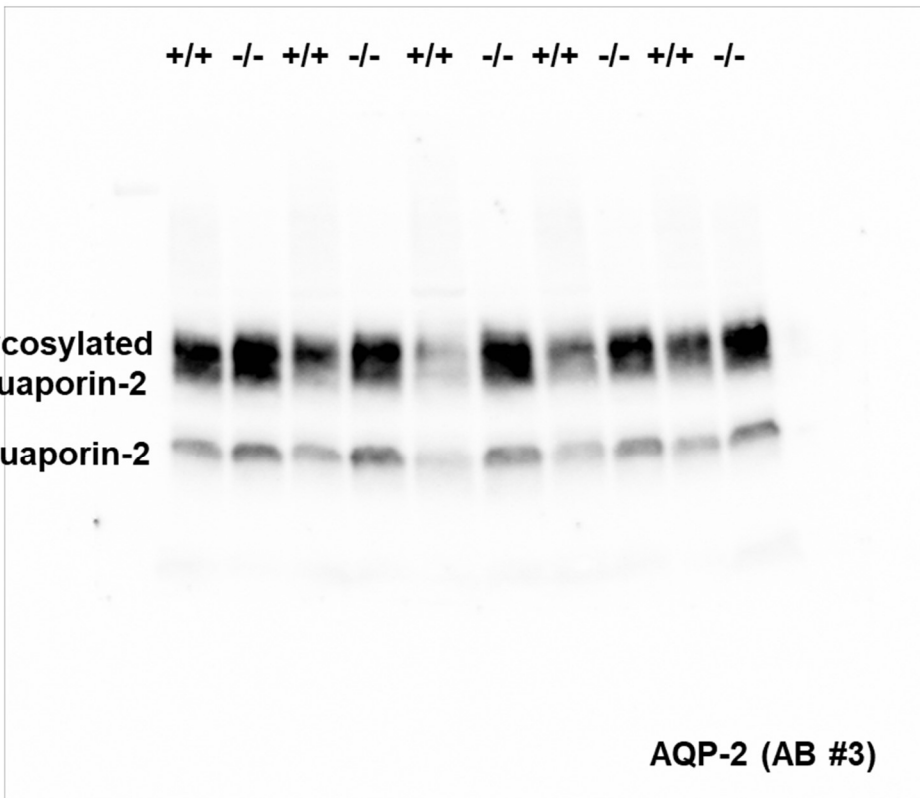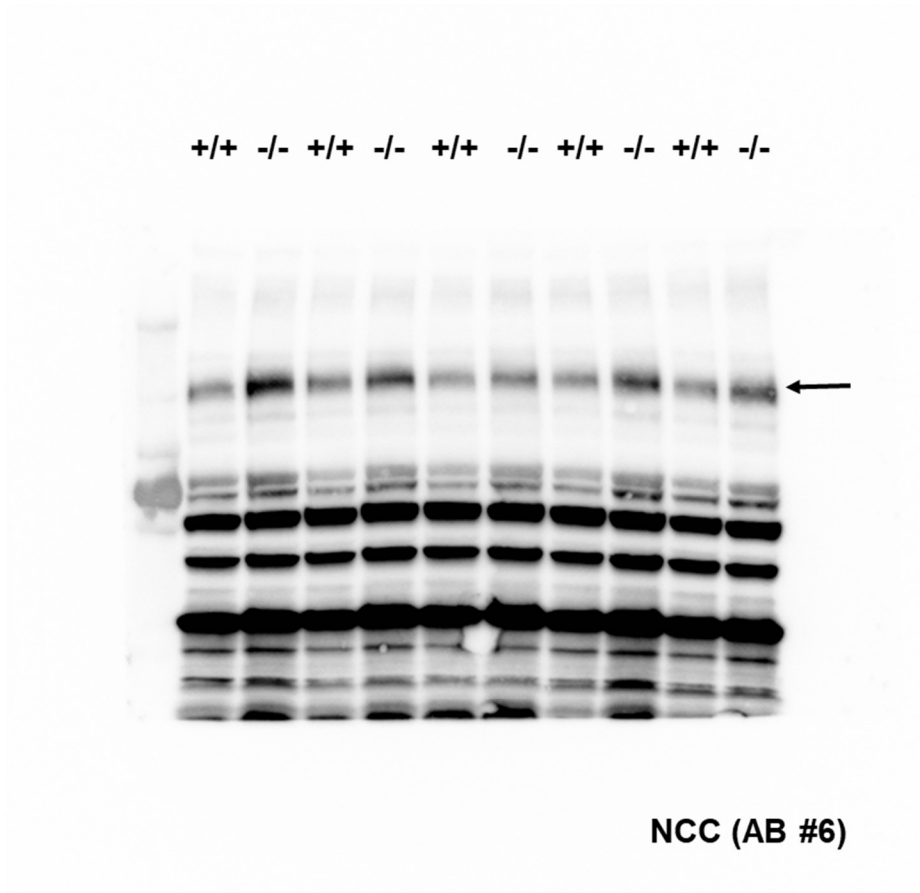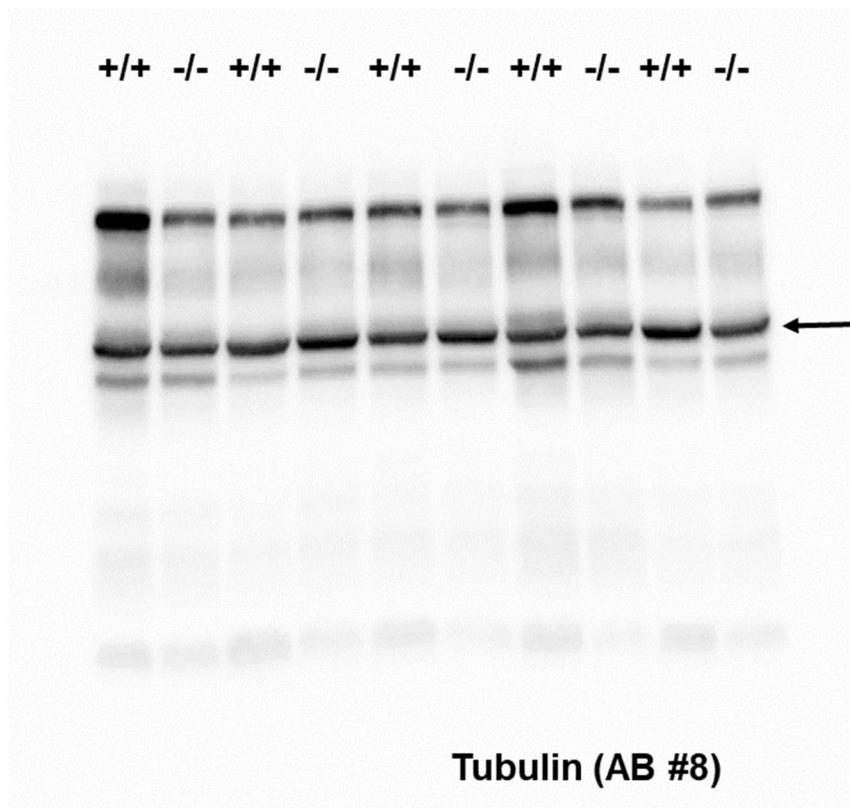
Original blots, Fig. 6

+/+ -/- +/+ -/- +/+ -/- +/+ -/- +/+ -/-

Claudin-10 (AB #2)

+/+ -/- +/+ -/- +/+ -/- +/+ -/- +/+ -/-

Claudin-2 (AB #1)

**Original blots, Supplemental Figure 9**
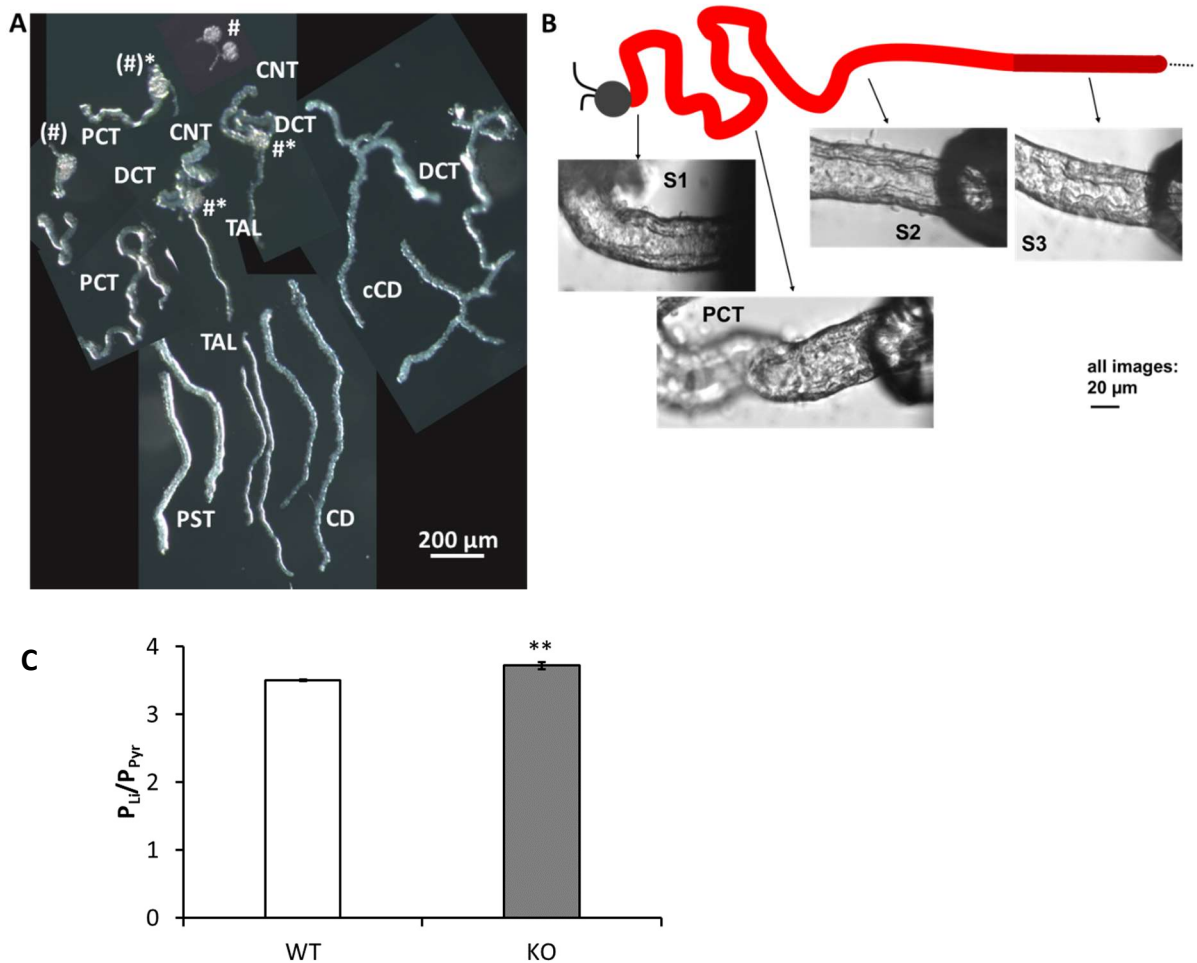
Supplemental Figure 5: Criteria for identification of tubular segments and permeability ratio P_{Li}/P_{Pyr}.

A Enzymatic preparation: glomeruli # − without remains of PT or TAL; vas afferens and efferens normally still attached; glomeruli with beginning S1 segment (#), PCT − long, shiny and smooth, no changes in diameter; PST (=PT S3) − very distinctive: thickest/broadest tubular segment, often milky, uniform cells, often slightly twisted with loose corkscrew like turns; TAL − very distinctive, shiny, thin; DCT − short, attached to TAL (MD, #*) or to CNT/CD, smooth, convoluted and shiny in the beginning; DCT2 and transition to CNT more variable; CNT/CD - branching, cobblestone like appearance (drainage points in cortical part).

B Localization of proximal segments for electrophysiological measurements with schematic proximal tubule (outer stripe of outer medulla in dark red).

C Permeability ratio P_{Li}/P_{Pyr} of isolated S2 segments: we assessed P_{Li}/P_{Pyr} in a subset of perfused PTs. The results showed an increase in paracellular lithium permeability in *Cldn10a* KO PTs, in line with the known Li permeability of *Cldn2*-based paracellular channels (Yu et al. J Gen Physiol 133: 111-127, 2009); **, $p < 0.01$.
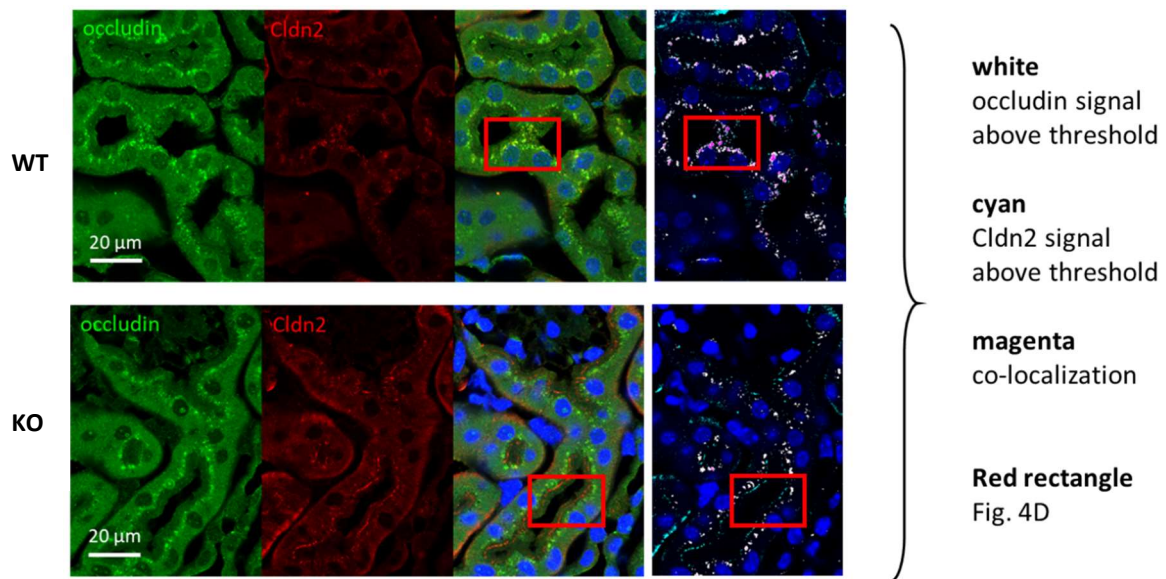
Supplemental Figure 6: Quantification of colocalization between occludin-positive vesicles and claudin-2.

To estimate co-localization between occludin-positive vesicles and claudin-2, images were recorded from regions predominantly containing S1 segments.

Left panels: Occludin, green, Claudin-2, red; nuclei in merged image, DAPI, blue.

Right panels: Intensity thresholds of 100 (total intensity range of 0 – 255) were chosen for both channels. Pixels with occludin intensities $\geq$ 100 and claudin-2 intensities <100 are visualized in white; pixels with occludin intensities <100 and claudin-2 intensities $\geq$ 100 are visualized in cyan; pixels with occludin and claudin-2 intensities $\geq$ 100 are visualized in magenta; DAPI, blue. Red rectangles are the image sections shown in Fig. 4D.
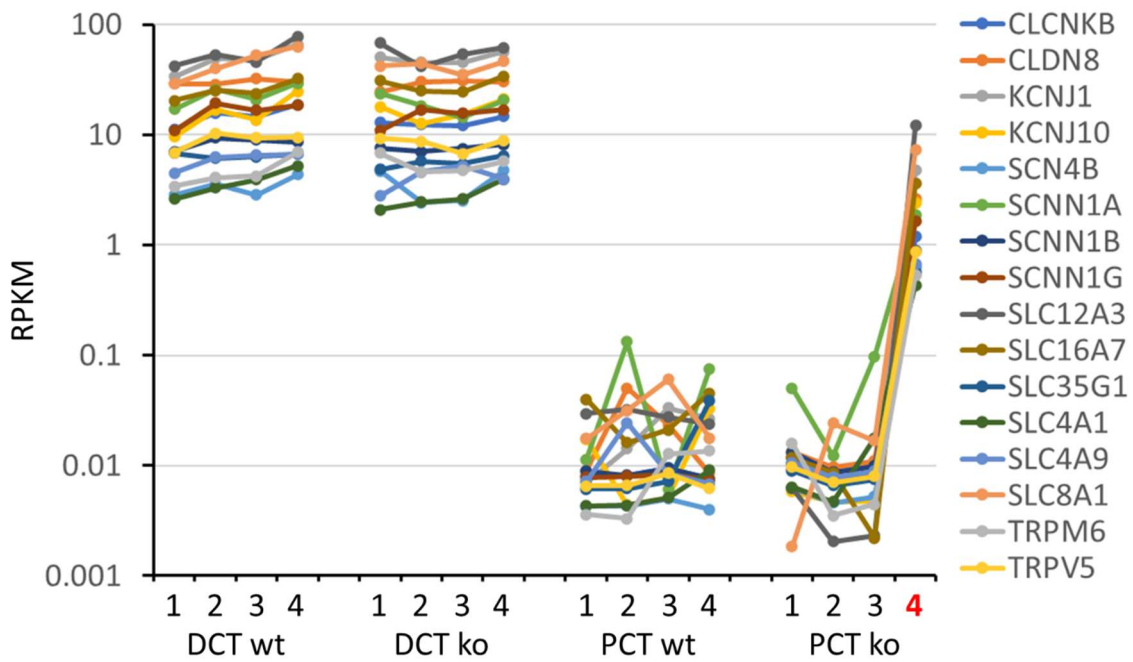
Supplemental Figure 7: Distal nephron segment contamination of *Cldn10a* KO PCT sample #4.

DCT and PCT nephron segments were collected from four WT and four *Cldn10a* KO kidneys and processed for RNA-Seq. RPKM (reads per kilobase of transcript, per million mapped reads) values for 16 genes are shown that are known to be highly expressed in DCT but low in PCT. For all of these genes, sample #4 from *Cldn10a* KO PCTs shows high RPKM values, indicating contamination of the sample with a more distal nephron segment. Consequently, this sample was excluded from further evaluation.
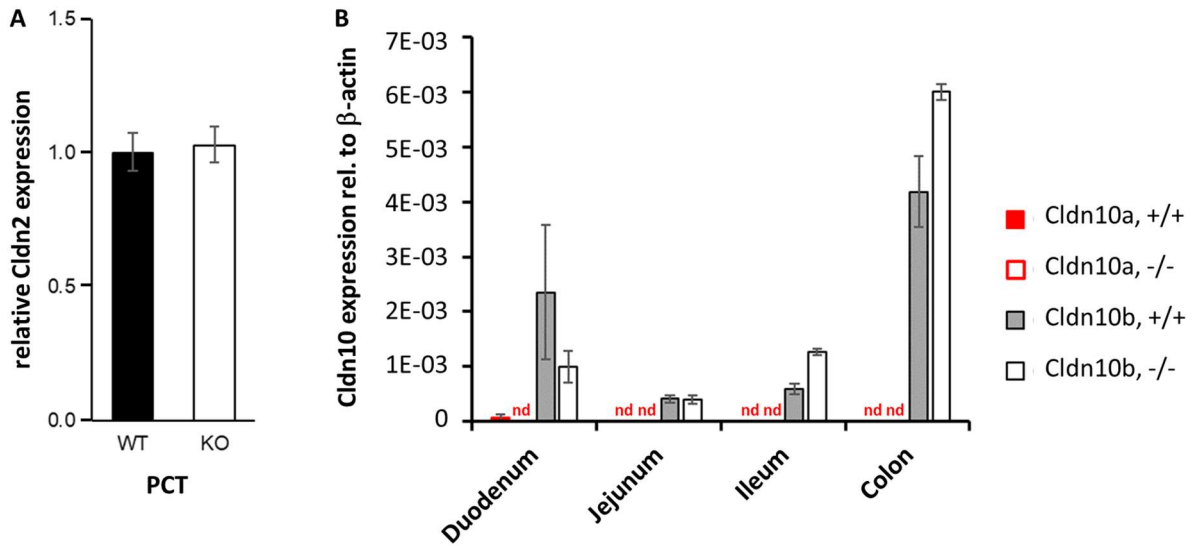
Supplemental Figure 8: Quantitative PCR.
A Relative *Cldn2* expression did not differ between isolated PCT from *Cldn10a* WT and KO animals.
B With the exception of negligible amounts in the duodenum of WT (+/+) mice, *Cldn10a* was not detected (nd) in the intestine of WT (+/+) and *Cldn10a* KO (-/-) mice. *Cldn10b* was present in all segments and no significant differences were detected between WT and *Cldn10a* KO animals.
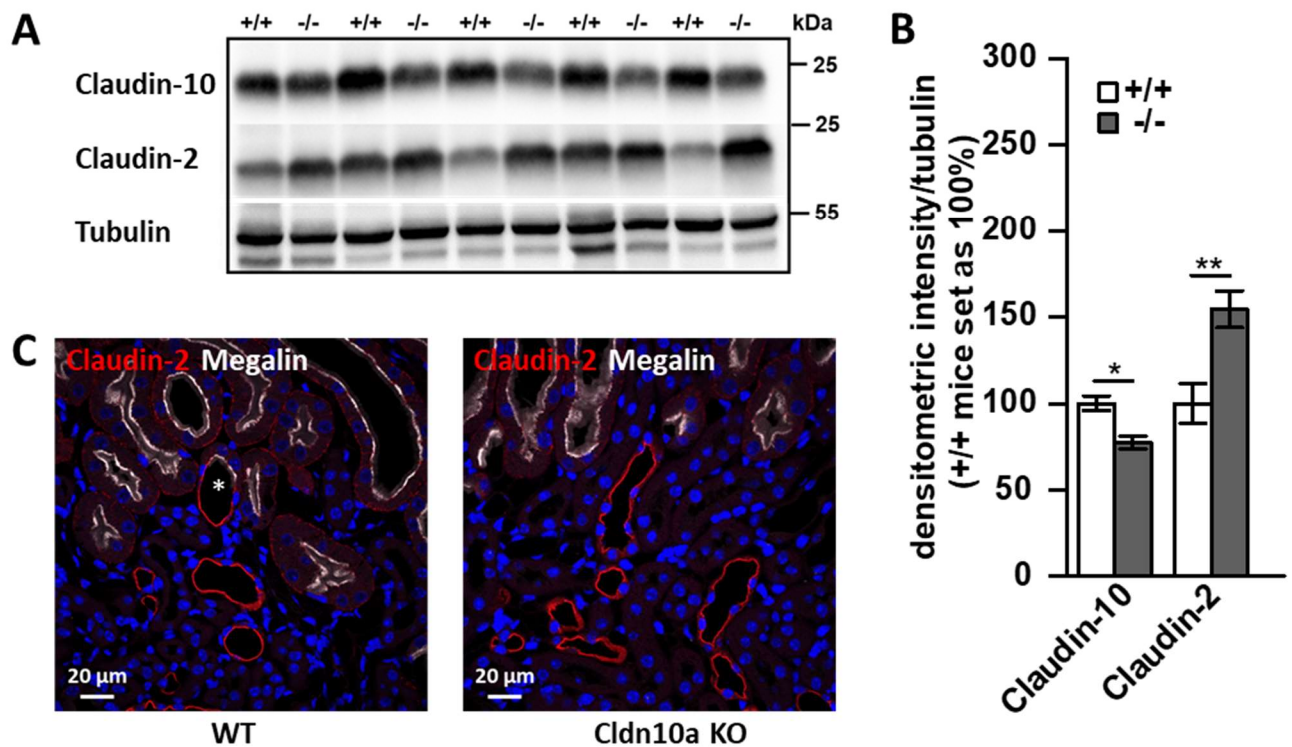
Supplemental Figure 9: Whole kidney claudin-2 and -10 Western blots, PT and non-PT claudin-2 staining.

A Claudin-10 signals in Western Blots of whole kidney protein extracts were reduced in *Cldn10a* KO (-/-) compared to WT (+/+) mice. The residual claudin-10 signal in -/- is due to claudin-10b, as the antibody does not discriminate between the two isoforms. Tubulin, loading control.
B Densitometric evaluation of the blot shown in **A**.
C Co-staining of claudin-2 (red) and megalin (gray) as PT marker in outer stripe of outer medulla. Megalin-positive tubules mark PT S3 segments. Very strong claudin-2 staining is observed in descending limbs of Henle's loop (megalin negative; * note continuity with S3 segment).
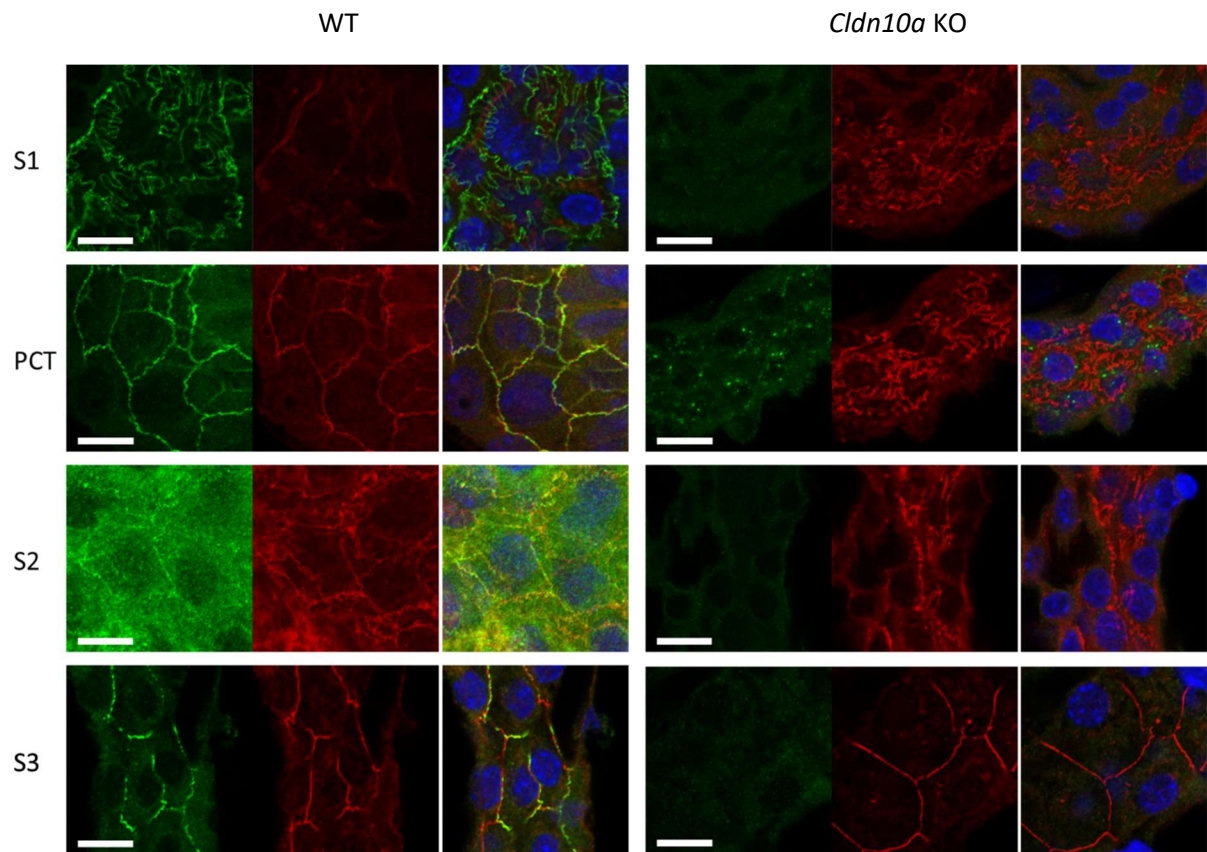
Supplemental Figure 10: Immunohistochemical staining of isolated proximal tubule segments.

Isolated WT and *Cldn10a* KO proximal tubule segments fixed and immuno-stained after dilution potential measurements (green, claudin-10; red, claudin-2; blue, DAPI; bars, 10 μm; merged channels also shown in Fig. 3C).

Supplemental Figure 11: RNA-Seq analysis.

A MA-Plot for PCT data. Genes with significantly altered expression levels are marked in red.

B Selection of overrepresented Gene Ontology annotations and their respective differentially expressed genes from the PCT data as heatmap. Fold change is color coded. For a complete list of enriched GO terms see Supplemental Table 8.

C Plot of $\log_2$-fold change between WT and *Cldn10a* KO DCT against the adjusted p-values. Red lines denote p = 0.05 and $|\log_2$-fold change$|$ = 1.5. None of $|\log_2$-fold change$|$ values exceeded the threshold of 1.5, and only three values exhibited p-values below 0.05:

AC134468.1, unknown function (ENSMUSG00000114147)

ATRX, chromatin remodeler, transcription modulator (ENSMUSG00000031229)

NAB1, Ngfi-A binding protein 1, transcription factor (ENSMUSG00000002881)

None of these genes bears any obvious direct relation to the phenotype of the *Cldn10a* KO mice.
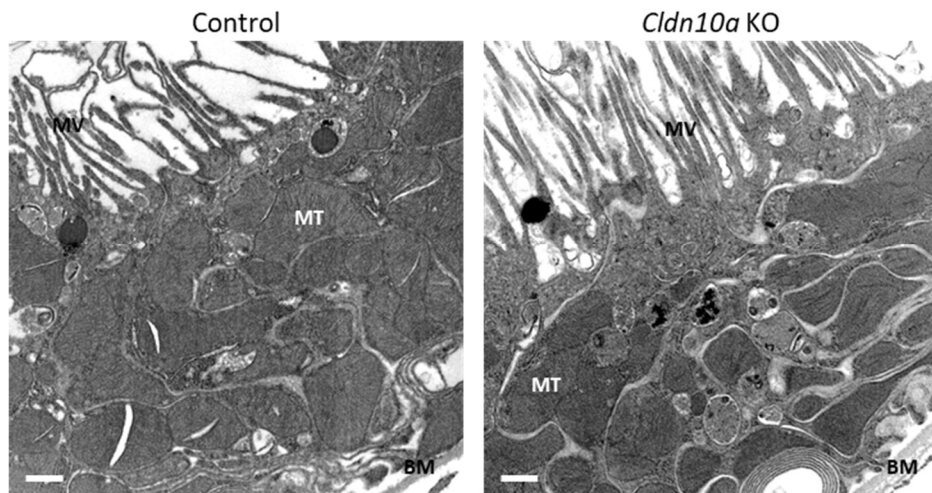
Supplemental Figure 12: Electron microscopy of PT mitochondria.

The morphology of PT mitochondria was not different between WT and *Cldn10a* KO mice in electron micrographs. Scale bars, 0.5 µm. BM, basement membrane; MT, mitochondrion; MV, microvilli.

Claudin-10a deficiency reduces Cl⁻ permeability and causes excessive proximal tubular cation selectivity via claudin-2 redistribution

JASN
JOURNAL OF THE AMERICAN SOCIETY OF NEPHROLOGY

METHODS

Claudin-10a specific knock-out mouse

Diffusion potential measurements in native proximal tubules

Expression data/protein biochemistry and gene expression profiling

Claudin-10
Claudin-2

Claudin-10 KO
Claudin-2

blood

Metabolic data
diuretic treatments

urine

OUTCOME

Proximal tubular axis

	S1	PCT (S1- S2)	S2	S3	
Claudin-10a - anion					localization in
Claudin-2 - cation					tight junction

P_{Cl}/P_{Na}

WT KO WT KO WT KO WT KO

PCl > PNa
PCl = PNa
PCl < PNa

P_{Na}/P_{Cl}

Claudin-10a KO
Claudin-2 - cation

localization in tight junction

→ Altered permeability + driving force → proximal + distal compensation → mild phenotype

shift paracellular → transcellular transport (energy consumption)

TAL DCT CD

upregulated downstream salt transport

P_{Mg} ↑
pH_{Urin} ↑

Conclusion

Claudin-10a is the major paracellular anion channel in the PT. Deletion causes imbalanced proximal tubular salt transport by recruitment of claudin-2 to the tight junction and triggers compensation mechanisms along the entire nephron.